The Canadian Meteorological Centre's Atmospheric Transport and Dispersion Modelling Suite

Réal D'Amours[1,*], Alain Malo[1], Thomas Flesch[2], John Wilson[2], Jean-Philippe Gauthier[1] and René Servranckx[1]

[1]*Environment Canada, Dorval, Quebec, Canada*
[2]*Centennial Centre for Interdisciplinary Science, University of Alberta, Edmonton, Alberta, Canada*

[Original manuscript received 5 May 2014; accepted 10 October 2014]

ABSTRACT *This paper describes the integrated suite of Lagrangian transport and dispersion models in operation at the Canadian Meteorological Centre. These models have been in use for several years and are applied to many types of environmental emergencies covering spatial scales from the very local to the global. The Modèle Lagrangien Courte Distance (MLCD) is used for atmospheric spills of the order of a few kilometres. The Modèle Lagrangien de dispersion de particules d'ordre 1 (MLDP1) is normally used for events affecting areas less than 100 km; Modèle Lagrangien dispersion de particules d'ordre zéro (MLDP0) is used for events of continental and global consequences. The Modèle Lagrangien dispersion de particules mode mixte (MLDPmm) alternates between first-order and zeroth-order depending on criteria specified by the user. The theoretical bases of the models are presented, and the main algorithms used in their implementation are discussed. Modelling of the diffusion processes is based on a stochastic differential equation with the assumption of quasi-stationary Gaussian turbulence, locally homogeneous in the horizontal. The practical aspects of the operational implementation are also described. Using these models, results from simulations of real cases on scales ranging from the very local, to a few kilometres, to regional (approximately 100 km) to continental (approximately 1000 km) and to global (approximately 10,000 km) are compared and validated with available observational data.*

RÉSUMÉ *Cet article décrit l'ensemble des modèles lagrangiens de transport et dispersion en exploitation au Centre météorologique canadien. Ces modèles sont employés depuis plusieurs années pour répondre à différents types d'urgences environnementales se produisant de l'échelle très locale jusqu'à l'échelle globale. Le MLCD (Modèle Lagrangien courte distance) est utilisé lors de déversements atmosphériques s'étendant sur quelques kilomètres. Le MLDP1 (Modèle Lagrangien de dispersion de particules d'ordre 1) est habituellement utilisé pour des évènements pouvant affecter des régions de dimensions inférieures à 100 km. Le MLDP0 (Modèle Lagrangien de dispersion de particules d'ordre 0) est utilisé pour des évènements ayant des conséquences continentales ou globales. Dans le MLDPmm (Modèle Lagrangien de dispersion de particules mode mixte), il y a alternance entre l'ordre zéro et l'ordre 1, selon des critères spécifiés par l'utilisateur. Les bases théoriques de ces modèles sont présentées, et les principaux algorithmes employés pour leur application sont examinés. La diffusion y est modélisée à l'aide d'une équation différentielle stochastique qui suppose une turbulence quasi-stationnaire, gaussienne, et localement homogène dans l'horizontale. Les aspects pratiques de l'implémentation opérationnelle sont décrits. Des résultats de simulations pour des incidents réels ayant des échelles très locales, quelques kilomètres, régionales, ∼100 km, continentales, ∼1000 km, et globales, ∼10000 km, sont montrés et comparés aux observations disponibles.*

KEYWORDS atmospheric dispersion; Lagrangian modelling; turbulent mixing; inverse dispersion modelling; emergency response

1 Introduction

The Canadian Meteorological Centre (CMC) is part of the Meteorological Service of Canada and is responsible for providing guidance on the transport and dispersion of dangerous substances released suddenly into the atmosphere. The various national and international environmental emergency response mandates assumed by the CMC cover scales ranging from the very local, to a few kilometres, to continental, and to global. For example, CMC provides guidance on the atmospheric dispersion of radioactive material in the framework of the Federal Nuclear Emergency Plan (FNEP) (Health Canada, 2014). The CMC also holds the following international designations:

*Corresponding author's email: damoursr@gmail.com

(1) Volcanic Ash Advisory Centre (VAAC) Montreal through the International Civil Aviation Organization (ICAO, 2004) and (2) Regional Specialized Meteorological Centre (RSMC) Montreal through the World Meteorological Organization (WMO) and the International Atomic Energy Agency (IAEA) (WMO, 2010, updated 2012).

To fulfill these mandates, an integrated suite of Lagrangian transport and dispersion models has been developed and implemented. These dispersion models have been used on a regular basis for several years in VAAC Montreal and RSMC Montreal to predict and track volcanic ash and gas (e.g., D'Amours et al., 2010; Simpson et al., 2002; Witham et al., 2007) as well as radioactive material released by nuclear accidents or tests (e.g., Becker et al., 2007; Draxler et al., 2015). The models are important tools for the contribution of the CMC to the Canadian response to nuclear emergencies and are regularly used for other environmental emergencies, such as smoke from forest fires, dust storms, toxic spills in the atmosphere, and chemical fires (e.g., Joly et al., 2010). The models can also be applied to the dispersion of viruses transported on aerosols (e.g., Gloster et al., 2010).

This paper presents the transport and dispersion models in operation at the CMC. The theoretical bases of the models as well as the practical aspects of their operational implementation are described in some detail in Sections 2 to 4. In Section 5, results from simulations of real cases using these models are compared and validated with available observational data.

2 Lagrangian modelling

In the context of Lagrangian modelling, dispersion in the atmosphere is estimated by calculating the trajectories of a very large number of air particles (or fluid elements) in order to adequately sample the dispersing plume. In general, these particles only differ from the other fluid elements because they are "marked." It is assumed that the marked particles conserve their identity during their flight. However, they can transport some amount of material that may be subject to various physical processes, such as dry deposition, wet scavenging, and radioactive decay. A particle can also be viewed as representing an ensemble of real particles. Upon release, it is assigned a mass that depends on the total quantity of the substance emitted and the total number of particles released, which has little to do with the real mass or size distribution of the aerosols represented.

In most applications, especially when considering transport on a regional or larger scale, the three-dimensional (3D) structure of the atmosphere and its evolution in time must be taken into account. For that reason dispersion models are usually executed with meteorological fields provided by a Numerical Weather Analysis and Prediction (NWP) system, in an "off-line" fashion. These fields are available only at specific time intervals and only at a limited number of discrete points in space (3D grids). Therefore, many scales of motion are not resolved. This is especially true of the turbulent components of the wind which are mostly responsible for the mixing of air parcels. The information provided by the NWP systems can be used to estimate at least some of the statistical features of the unresolved scales and of atmospheric turbulence. Lagrangian Stochastic Models (LSMs) use a stochastic differential equation (SDE) to calculate a probable trajectory for a given particle based on these statistics.

The application of Monte Carlo methods to simulate dispersion in simple cases, by calculating the trajectory of several particles, started in the early 1970s (Thompson, 1971; Thomson & Wilson, 2012). However, the idea of considering diffusion in the Lagrangian framework goes back to the beginning of the twentieth century (Langevin, 1908) and, in the context of atmospheric diffusion, to the 1920s (Krasnoff & Peskin, 1971; Taylor, 1922). J. D. Wilson, Thurtell, and Kidd (1981b) and J. D. Wilson, Legg, and Thomson (1983) successfully applied Monte Carlo methods to dispersion, using a formulation of turbulent motion statistics based on realistic models of the atmospheric surface layer for different stability regimes. They compared the results with data from the Prairie Grass Experiment (Project Prairie Grass; Barad, 1958). Their model was later formalized by Thomson (1984, 1987).

3 Accounting for turbulent mixing

a *A First-Order Model for the Particle Velocities*

Representing the real wind experienced by a particle as $U_i + u'_i$, where U_i is the resolved or large-scale component usually provided by the NWP models, and u'_i is the unresolved fluctuating part, then the following SDE provides the basis for the evolution of the unresolved u'_i component (J. D. Wilson & Sawford, 1996):

$$du'_i = a_i\,dt + b_{ij}\,d\xi_j\,, \tag{1}$$

where the terms a_i and b_{ij} (Einstein summation convention is used) are functions of time and space, and $d\xi_j$ is Gaussian white noise, with zero mean and $(dt)^{1/2}$ standard deviation. The change in the particle's position is then evaluated:

$$dx_i = (U_i + u'_i)\,dt\,. \tag{2}$$

Thomson (1987) discussed possible criteria for the determination of the a_i and b_{ij} terms. He recognized that they could essentially be subsumed under one criterion which he called "the well-mixed condition (wmc)": an initially well-mixed set of particles in a fluid (i.e., they are distributed in phase-space—position and velocity—as are all the other fluid particles) will remain well mixed. He also indicated that this criterion did not lead to a unique determination of the a_i and b_{ij} coefficients in Eq. (1).[†]

[†]Unless it so happens that the model is one-dimensional, or the different velocity fluctuation components are independent.

Consistency with Kolmogorov similarity theory for locally isotropic turbulence allows the determination of the b_{ij} coefficients (Thomson, 1987):

$$b_{ij} = \sqrt{\varepsilon C_0}\delta_{ij}\,, \tag{3}$$

where ε is the local turbulent kinetic energy (TKE) dissipation rate, C_0 a putatively universal constant, and δ_{ij} the Kronecker delta function.

Neglecting the turbulent velocity covariances, and assuming quasi-stationary Gaussian turbulence, locally homogeneous in the horizontal, an expression for the coefficients a_i can be derived:

$$a_u = -\frac{C_0\varepsilon}{2\sigma_u^2}u' + \frac{1}{2\sigma_u^2}\frac{\partial\sigma_u^2}{\partial z}u'(w'+W)\,, \tag{4}$$

$$a_v = -\frac{C_0\varepsilon}{2\sigma_v^2}v' + \frac{1}{2\sigma_v^2}\frac{\partial\sigma_v^2}{\partial z}v'(w'+W)\,, \tag{5}$$

$$a_w = -\frac{C_0\varepsilon}{2\sigma_w^2}w' + \frac{1}{2\sigma_w^2}\frac{\partial\sigma_w^2}{\partial z}w'(w'+W) + \frac{1}{2}\frac{\partial\sigma_w^2}{\partial z}\,, \tag{6}$$

where the usual 3D definition (x, y, z, u, v, w) is used. The turbulent velocity variances are σ_u^2, σ_v^2, and σ_w^2 and W represents large-scale vertical motion. The discretized form of this set of equations constitutes the basis of the first-order dispersion models implemented at CMC.

b *The Random Displacement Model*

Dispersion models based on the equations in Section 3a are called first-order models because they relate to particle velocities. One of the constraints of a discretized first-order model is that the time steps must be much smaller than the Lagrangian time scale for turbulence T_L (i.e., the particle velocity de-correlation time) which can be expressed as $2\sigma_w^2/C_0\varepsilon$. For turbulent eddies generally associated with atmospheric diffusion, this time scale can be of the order of a minute in the middle of a fully developed boundary layer (Hanna, 1981) and much smaller close to the ground where TKE dissipation rates can be very large.

Although a first-order LSM is required to properly calculate the velocity of the particles as they move through the turbulent eddies, in large-scale dispersion applications one may not be interested in the precise details of the concentration field very close to the source. Rodean (1996) derived a Random Displacement Equation (RDE) by integrating the Lagrangian stochastic equation (LSE) over a time interval larger than T_L. This can be regarded as taking the diffusion limit of the first-order LSM (Durbin, 1980). Boughton, Delaurentis, and Dunn (1987) also emphasized the equivalence of the Eulerian advection–diffusion equation with the RDE. However, the connection between the diffusion equation and a random walk had long been known in physics. Considering the vertical component, the RDE is written as

$$dz = \left[\frac{\partial K_z}{\partial z} + W\right]dt + \sqrt{2K_z}\,d\xi \tag{7}$$

$$K_z = \sigma_w^2 T_L \tag{8}$$

where K_z represents a vertical diffusion coefficient, W is the large-scale (synoptic) vertical motion, and $d\xi$ again is a Gaussian random number with mean of zero and variance dt. Because the RDE is applied to displacements, it is called a zeroth-order equation or model, in contrast to first-order models. The main advantage of the RDE is that it allows for longer time steps than the discretized Langevin equation for particle velocities (J. Wilson & Yee, 2007).

4 CMC's dispersion modelling suite: MLCD, MLDP1, MLDP0 and MLDPmm, and the trajectory model

A suite of dispersion model codes for environmental emergency response has been implemented at the CMC. A short-range model, Modèle Lagrangien Courte Distance (MLCD) is used for dispersion events having impacts at distances of one to ten kilometres. The Modèle Lagrangien de dispersion de particules d'ordre 1 (MLDP1) is mainly used for regional-scale problems (domains of the order of 100 km or less), and the Modèle Lagrangien de dispersion de particules d'ordre zéro (MLDP0) is used for dispersion events having continental or global impacts. It is possible to switch from the MLDP1 kernel to the MLDP0 kernel within one simulation based on a criterion such as the age of a particle. It is also possible to produce simulations in mixed mode, within the MLDP1 kernel, switching from one mode to another according to specific criteria, and this is referred to as MLDPmm. However, the diffusion coefficient in MLDPmm differs from that of MLDP0.

To minimize the pre-processing of this meteorological input, the structure of CMC dispersion models is closely matched to those of the driving meteorological numerical analysis and forecast models. For example, they operate in the same vertical coordinate and use the same formulation for vertical motion; MLDP1 normally uses the NWP TKE. The meteorological data required to drive the models are provided by CMC's NWP system. For the global scale, the data come from the CMC Global Deterministic Prediction System (GDPS; Canadian Meteorological Centre, 2013a) which is based on global 4D-Var data assimilation coupled to the Global Environmental Multiscale (GEM) forecast model having a horizontal resolution of approximately 25 km and 79 vertical levels. For the continental scale, the data are provided by the Regional Deterministic Prediction System (RDPS; Canadian Meteorological Centre, 2013b), also based on regional 4D-Var assimilation coupled to a limited area forecast model with a horizontal resolution of 10 km on a 996×1028 grid and a vertical configuration similar to that of the GDPS. The GDPS executes twice a

day, and the RDPS executes four times each day. The CMC also operates a High Resolution Deterministic Prediction System (HRDPS; Canadian Meteorological Centre, 2011) at a horizontal resolution of 2.5 km, on five windows covering specific sectors of Canada.

a *MLCD*

The function of the MLCD is to provide a quick estimate of the dispersion of a plume at local scales that would allow the input of local meteorological information and observations when available. The MLCD is also a first-order Lagrangian stochastic model based on the same equations as MLDP1. As well, the same parameterization is used to estimate the three components of the turbulent velocity variance. The meteorological conditions are assumed to be uniform in the horizontal over all the MLCD domain. Even though stationarity is an assumption underlying the Lagrangian stochastic equations used in MLCD, the meteorology is allowed to change with time presuming, as with MLDP1, that the time scale of these changes is large compared with the turbulence time scale.

The MLCD is supplemented with an average wind model needed to generate a vertical wind profile and other parameters describing the boundary layer (J. D. Wilson & Flesch, 2004). This profile is obtained by matching the Monin-Obukhov surface layer profile to a baroclinic Ekman profile in the upper portion of the boundary layer. The resulting profile is adjusted—best fitted—to any meteorological information provided by the user (at least one wind datum). An often-used procedure is to provide the wind model with a surface wind observation together with estimates of the horizontal wind in the upper portion of the boundary layer provided by NWP models. In that case, estimates of the Monin-Obukhov length L (defined below) and of the boundary layer height H have to be provided.

b *Estimation of the Velocity Variances for MLDP1*

1 USING BOUNDARY LAYER PARAMETERS PROVIDED BY NWP MODELS

The TKE (denoted by E) provided by the CMC NWP models represents the sum of all the velocity variances (Bélair, Mailhot, Strapp, & MacPherson, 1999; Mailhot & Benoit, 1982):

$$E = \frac{1}{2}(\sigma_u^2 + \sigma_v^2 + \sigma_w^2)\,. \tag{9}$$

Therefore, E has to be partitioned into its three components in order to solve Eqs (4) to (6). Assuming that the horizontal variances $\sigma_u^2 = \sigma_v^2$, denoted by σ_{uv}^2, the partitioning is done by calculating ratios (m_{uv}, m_w) that are applied as factors to the E provided by the NWP models as follows:

$$\sigma_{uv}^2 = 2m_{uv}E \tag{10}$$

$$\sigma_w^2 = 2m_wE \tag{11}$$

with the constraints $2m_{uv} + m_w = 1$ and $2\sigma_{uv}^2 + \sigma_w^2 = 2E$ giving

$$m_{uv} = \frac{\sigma_{uv}^2}{2\sigma_{uv}^2 + \sigma_w^2} \tag{12}$$

$$m_w = \frac{\sigma_w^2}{2\sigma_{uv}^2 + \sigma_w^2}\,. \tag{13}$$

Boundary layer parameterizations suggested by Nieuwstadt (1984), Weil (1990) and Rodean (1996) are used to estimate the portion each component contributes to the total variance. A ratio is calculated and applied as a factor to the TKE provided by the NWP models.

For the unstable case, when the Monin-Obukhov length scale L is negative

$$\sigma_{uv}^2 = u_*^2\left[4.5\left(1-\frac{z}{h}\right)^{3/2} + 0.6\left(-\frac{h}{L}\right)^{2/3}\right] \tag{14}$$

$$\sigma_w^2 = u_*^2\left[\left(1.6-\frac{z}{h}\right)^{3/2} - \frac{3z}{L}\left(1-0.98\frac{z}{h}\right)^{3/2}\right]^{2/3}, \tag{15}$$

where u_* is the friction velocity, z the height above ground, and h the depth of the boundary layer. For the stable case where $L \geq 0$

$$\sigma_{uv}^2 = 4.5u_*^2\left(1-\frac{z}{h}\right)^{3/2} \tag{16}$$

$$\sigma_w^2 = 1.96u_*^2\left(1-\frac{z}{h}\right)^{3/2}. \tag{17}$$

These variances are only used to estimate how the NWP TKE (denoted here as $\tilde{E}$) should be partitioned between the various components. Using the ratios from Eqs (12) and (13)

$$\tilde{\sigma}_{uv}^2 = 2m_{uv}\tilde{E} \tag{18}$$

$$\tilde{\sigma}_w^2 = 2m_w\tilde{E}. \tag{19}$$

This is done because it should not be expected that the estimates of E resulting from the sum of the variances given by the parameterizations will equal $\tilde{E}$; however, it is assumed that $\tilde{E}$ provides a better representation of the real TKE and, consequently, $\tilde{\sigma}_{uv}^2$ and $\tilde{\sigma}_w^2$ provide a better representation of the real turbulent wind variances.

2 ESTIMATION OF L AND u_*

When $\tilde{E}$, the NWP TKE, is not available, for example in diagnostic mode where one uses meteorological fields from objective analyses, the parameterizations of Eqs (14) to (17) are used directly. In that case L and u_* are also needed. Estimates are obtained from the low level horizontal wind profile,

assuming that the two lowest levels at which the winds are available, approximately 10 and 40 m, are within the surface layer. Following Monin-Obukhov similarity theory, the wind and potential temperature vertical gradients are expressed in terms of universal functions ϕ_m and ϕ_h of the non-dimensional height $\zeta = z/L$:

$$\frac{\partial U}{\partial z} = \frac{u_*}{kz}\phi_m\left(\frac{z}{L}\right), \tag{20}$$

$$\frac{\partial \theta}{\partial z} = \frac{T_*}{kz}\phi_h\left(\frac{z}{L}\right), \tag{21}$$

$L = -u_*^3\theta_0/kgQ_0$ is the Monin-Obukhov length scale, where k is the von Karman constant, θ_0 and Q_0 are, respectively, the potential temperature and kinematic heat flux density very close to the ground, u_* is the friction velocity, and $T_* = -Q_0/u_*$; L can also be written as $u_*^2\theta_0/kgT*$. There are no physical theories to help in the formulation of the functions ϕ_m and ϕ_h; they have to be determined experimentally. Based on the Kansas field experiment (Haugen, Kaimal, & Bradley, 1971), Businger, Wyngaard, Izumi, and Bradley (1971) obtained the following expressions:

$$\phi_m = \begin{cases} (1-15\zeta)^{-1/4} & \zeta < 0 \\ 1+4.7\zeta & \zeta \geq 0 \end{cases}, \tag{22}$$

$$\phi_h = \begin{cases} 0.74(1-9\zeta)^{-1/2} & \zeta < 0 \\ 0.74+4.7\zeta & \zeta \geq 0 \end{cases}. \tag{23}$$

The formulation for the unstable case, $\zeta < 0$, was later revised by Dyer and Bradley (1982) to

$$\phi_m = (1-28\zeta)^{-1/4}, \tag{24}$$

$$\phi_h = (1-9\zeta)^{-1/2} \tag{25}.$$

Expressing the vertical gradients of U and θ in Eqs (20) and (21) in terms of finite differences between the two lowest model levels and using the formulations of Dyer and Bradley (1982) for $\zeta \leq 0$ and of Businger et al. (1971) for $\zeta > 0$, an estimate of u_* and T_* is obtained by iteration, using the gradient Richardson number Ri:

$$\mathrm{Ri} = \frac{g}{\theta_v}\frac{\partial\theta_v/\partial z}{(\partial U/\partial z)^2 + (\partial V/\partial z)^2}, \tag{26}$$

as a first guess for ζ.

c *Estimation of the Diffusion Coefficient K_z*

The importance of vertical wind shear in horizontal diffusion is well known (Smith, 1965; J. D. Wilson, Flesch, & Swaters, 1993), and experience has shown that most of the lateral spread of a plume in the boundary layer results from the combined effects of vertical mixing and vertical wind shear (Ekman spiral). For that reason, only vertical diffusion is considered when executing the MLDP0 kernel. According to Eq. (8), $K_z = \sigma_w^2 T_L$. In NWP models, K_z is more often written in terms of a length scale (a mixing length). In CMC NWP models, K_z is modelled as $a\lambda E^{1/2}$ where a is a constant, λ a mixing length, and E the TKE (Bélair et al., 1999).

When available, this vertical diffusion coefficient can be used. However, this is not usually the case in diagnostic mode. In MLDP0, K_z is simply calculated using the O'Brien (1970) function:

$$K = K(h) + \left[\frac{(h-z)}{(h-h_{\mathrm{sl}})}\right]^2 \left\{K(h_{\mathrm{sl}}) - K(h) + (z-h_{\mathrm{sl}})\left[\left.\frac{\partial K}{\partial z}\right|_{h_{\mathrm{sl}}} + 2\frac{K(h_{\mathrm{sl}})-K(h)}{h-h_{\mathrm{sl}}}\right]\right\}, \tag{27}$$

where $h_{sl} \leq z \leq h$, h_{sl} being the height of the surface layer and h, the height of the boundary layer. Following Delage (1988), the height of the first level above ground of the driving NWP model is taken as the top of the surface layer h_{sl}. At this level K_z is calculated in terms of a mixing length, stability function, and vertical shear of the horizontal wind vector $\mathbf{U}$, according to Delage (1997):

$$K(h_{\mathrm{sl}}) = \frac{(k\,h_{\mathrm{sl}})^2}{\phi_m\phi_h}\left|\frac{\partial \mathbf{U}}{\partial z}\right| \tag{28}$$

and

$$\phi_m\phi_h = \begin{cases} \beta(1+12\mathrm{Ri})^2 & \mathrm{Ri} > 0 \\ \beta(1-40\mathrm{Ri})^{1/2} & \mathrm{Ri} \leq 0 \end{cases} \tag{29}$$

where Ri is the gradient Richardson number and k the von Karman constant. The stability functions ϕ_m and ϕ_h are identical to those used in CMC's GEM model (Mailhot et al., 1998). The boundary layer height h is provided by the NWP model or is diagnosed from the wind and temperature fields as the height at which the bulk Richardson number reaches a critical value (0.25). In MLDPmm K_z is expressed as $\sigma_w^2 T_L$.

d *Effect of the Vertical Density Gradient in the Atmosphere*

Thomson's well-mixed condition, mentioned in Section 2, requires that dispersion models do not change with time, and the distribution in phase space of tracer particles is initially distributed like all the other fluid particles in which they are immersed. The set of stochastic equations shown in Section 3a (Eqs (4) to (6)), will tend to distribute particles uniformly in the vertical, while the actual atmospheric air density ρ decreases with height. The net effect would be more tracer particles relative to the other fluid particles at upper levels and the reverse at lower levels. The difference may not be important within a shallow boundary layer but can become

non-negligible when the top of the boundary layer top is well over a kilometre. Stohl and Thomson (1999) proposed the addition of the following term to Eq. (6):

$$\frac{\sigma_w^2}{\rho}\frac{\partial \rho}{\partial z}. \tag{30}$$

Such a term has been added to MLDP1. A similar correction was derived for the RDE:

$$\frac{K_z}{\rho}\frac{\partial \rho}{\partial z} \tag{31}$$

and has been implemented in MLDP0. In the first-order model, term (30) is an acceleration that is proportional to the vertical velocity variance and tends to accelerate the particle down the density gradient (i.e., downward in the hydrostatic atmosphere). Term (31) acts as a drift velocity, proportional to the diffusion coefficient, and also tends to move the particle downward.

e *Horizontal Diffusion*

The presence of fluctuations or intermittency at time scales larger than those of atmospheric turbulence has been under investigation for some time (Gupta et al., 1997; Hanna, 1986) and has been attributed to horizontal wind fluctuations of periods of a few hours, also known as meandering. In order to simulate the average effect of this process, a first-order Langevin equation has been included, similar to Maryon (1998):

$$du_m = -\frac{u_m}{\tau_m}dt + \sqrt{\frac{2\sigma_{u_m}^2}{\tau_m}}d\xi, \tag{32}$$

where u_m is the u component of the meandering velocity, τ_m the time scale, and $\sigma_{u_m}^2$ the variance of these fluctuations. Here again, $d\xi$ is a Gaussian random number with a mean of zero and variance dt. The v component of the meandering velocity is modelled with an identical equation. The determination of τ_m and $\sigma_{u_m}^2$ is empirical, and these parameters are input by the user.

f *Dispersion at the Top of and Above the Boundary Layer*

Vertical mixing is greatly reduced at the top of the boundary layer because of the presence of a thermally stable layer which dampens the turbulence. Although the ground surface constitutes an absolute boundary, there is no material lid at the top of the boundary layer to prevent particles from moving back and forth. The transition zone at the top of the boundary layer can be very thin but can fluctuate considerably in space and time (Wyngaard, 2010). Temporal and/or spatial averaging will depict a layer where exchanges between the boundary layer and the free troposphere (FT) above occur. This layer is often called the entrainment zone (EZ) (Crum & Stull, 1987). Near the top of the boundary layer, the variance of the vertical velocities σ_w^2 decreases as the TKE decreases. The TKE dissipation rate ε also decreases but faster than the TKE itself,[†] so that T_L increases. Therefore, the constraint on the time step is less stringent and particles could cross the boundary layer top simply because of numerical effects. Even though there is transport or entrainment across the EZ, transport resulting strictly from diffusion is often considered negligible. Particles that would move above the top are reflected downward (e.g., Stohl, Forster, Frank, Seibert, & Wotawa, 2005). Such a reflection is implemented in the MLDP0 kernel and in MLCD. Transfer between the boundary layer and the FT can occur through other mechanisms. For example, particles that were in the FT may become "entrained" in the boundary layer if it rises above their vertical position during the simulation; conversely, particles may be left in the FT if the boundary layer lowers below their position. Also in MLDP0, the synoptic vertical motion can move particles across the top of the boundary layer. In the MLDP1 kernel, there is no imposed reflection at the top of the boundary layer, and particles follow the trajectories dictated by the 3D winds and the ambient TKE.

There is no dominant mechanism producing mixing in the FT. Turbulence is rather localized in time and space and can be generated locally by gravity waves or deep convection. Very often, substances injected above the boundary layer travel in fairly well-maintained streams for several days (Colette, Menut, Haeffelin, & Morille, 2008; D'Amours, Mintz, Mooney, & Wiens, 2013; Gerasopoulos et al., 2006). In MLDP0, the vertical diffusion coefficient falls to a very low threshold value in the FT and the RDE is essentially turned off. Nevertheless, there can still be a reasonable amount of dispersion induced by stretching and deformation in the horizontal wind and by vertical transport associated with large-scale dynamics. Furthermore there is also the option of activating the lateral diffusion discussed in Section 4e.

g *Near the Surface*

1 SURFACE REFLECTION

The average wind vanishes at height z_0, the roughness length. Near this level the length scale of the turbulent eddies decreases, the TKE dissipation rate ε increases, and the Lagrangian time scale T_L decreases. The problems arising from the treatment of this boundary condition in the context of a discretized Langevin equation like Eq. (1) were discussed in detail by J. D. Wilson and Flesch (1993). Their concept of an unresolved basal layer (UBL) is used in MLDP1 and MLCD. A perfect reflection is applied to a particle that would enter the UBL. Depending on the depth of the UBL, the particle is required to wait a specified amount of time

[†]In CMC NWP models $\varepsilon \propto E^{3/2}$.

during which it will drift horizontally in the direction of the surface layer wind, following the UBL model described by J. D. Wilson, Flesch, and d'Amours (2001). The height of the UBL is chosen by the user based on practical considerations, the main one being the length of the time step constrained by the Lagrangian time scale.

2 DRY DEPOSITION

Dry deposition is assumed to occur when a particle representing a tracer that could be absorbed or captured by surface elements enters the UBL. An absorption probability P is calculated according to J. Wilson, Ferrandino, and Thurtell (1989):

$$P = 1 - R \tag{33}$$

$$R = \frac{1-a}{1+a}; \quad a = \left(\frac{\pi}{2}\right)^{1/2} \frac{v_d}{\sigma_w},$$

where R is the reflection probability, v_d is the dry deposition velocity, and σ_w the standard deviation of the vertical turbulent wind component. In MLDP0, σ_w is approximated in terms of the variance of the discrete random vertical displacements, which following the RDE, Eq. (7), is given by:

$$\overline{\Delta z^2} = 2K_z \Delta t$$

$$\sigma_w \approx \frac{\sqrt{\overline{\Delta z^2}}}{\Delta t} = \sqrt{\frac{2K_z}{\Delta t}}. \tag{34}$$

Because a model particle represents an ensemble of particles in the atmosphere, the modelled effect of dry deposition is to reduce the particle mass by a fraction given by P. This process is different from deposition due to gravitational settling.

h *Gravitational Settling*

Generally in Lagrangian modelling, the "marked" particles are not really different from the other fluid elements and they follow similar trajectories. However, when modelling heavy particulates subject to gravitational acceleration, the LSE and RDE are no longer valid. The simplest approach is to add a gravitational settling velocity W_g to the vertical component of Eq. (2) or to the synoptic vertical motion W in Eq. (7), and to consider that a model particle is an ensemble of those particulates. This approach is implemented in the CMC dispersion models.

J. D. Wilson, Thurtell, and Kidd (1981a) proposed a similar modification to their LSE. They compared their model results with data from an experiment they performed using monodispersed glass beads and showed that it worked satisfactorily. J. D. Wilson (2000) reviewed various stochastic models for heavy particle dispersion, including one based on the modified RDE, comparing model results with experimental data. The conclusion was that no significant increase in accuracy is obtained by using models more complex than Eq. (2) plus W_g. The model based on the RDE did not perform very well at distances very close to the release point but was adequate at distances beyond 200 m.

At CMC, the modelling of gravitational settling is mostly used for tracking volcanic ash plumes. In that case the settling velocity of ash particles is simply modelled in terms of Stokes law for spherical particles following Sparks et al. (1997, p. 384):

$$W_g = \frac{g\rho_{\text{ash}} d^2}{18\nu\rho_{\text{air}}}, \tag{35}$$

where g is the acceleration due to gravity, ρ_{ash} and ρ_{air} are, respectively, the ash and air densities, d is the diameter of the spherical ash particle, and v is the air kinematic viscosity. Because the size distribution of the ash particles is highly dependent on the magma characteristics and the eruption type, a few empirical distributions, such as those proposed by Durant and Rose (2009), are available to the user.

i *Wet Scavenging Radioactive Decay*

In CMC's dispersion models the removal of aerosols by clouds and precipitation is modelled in a rather crude fashion because a good specification of the 3D precipitation rate fields is seldom available in diagnostic mode, especially over the oceans. Simply, wet scavenging occurs when a particle is presumed to be in clouds. The fractional cloud cover f_c is estimated with a simple function of the local relative humidity U and a threshold value U_0:

$$f_c = \begin{cases} 0 & U < U_0 \\ \dfrac{U - U_0}{1 - U_0} & U \geq U_0 \end{cases}. \tag{36}$$

The tracer loss rate experienced by a fluid element is proportional to the cloud fraction and the particle tracer mass m_p:

$$\left.\frac{\partial m_p}{\partial t}\right|_{w_s} = -(f_c w_s) m_p t, \tag{37}$$

where w_s is an empirical wet scavenging factor.

A more realistic physical parameterization (Feng, 2007) can be activated when precipitation rate fields are available.

Tracer loss rate resulting from radioactive decay is calculated using the standard formulation:

$$\left.\frac{\partial m_p}{\partial t}\right|_r = -\ln(2)\, m_p \, \frac{t}{t_{1/2}}, \tag{38}$$

where $t_{1/2}$ is the half-life of the tracer species characterizing the particle and m_p its mass. The fate of the elements resulting from the decay is not modelled. The possible in-growth from the decay of other radioactive tracers is also not taken into account.

j *Concentration Estimation*

Although LSMs yield particle trajectories, it is concentration fields and concentrations at specific locations that are needed most of the time. Assuming that the particle "mass" is given by m_p, an estimation of the concentration field is obtained by counting the number of particles in each of the cells of a 3D array covering the domain of interest. The concentration at point $\mathbf{r}$ is simply:

$$c(\mathbf{r}, t) = \frac{1}{\delta V_s} \sum_{p \varepsilon \delta V_s} m_p(\mathbf{r}, t), \tag{39}$$

where δV_s is the volume of the cell centred on $\mathbf{r}$. A justification of this approach is given in Appendix A.

k *Inverse Modelling*

Flesch, Wilson, and Yee (1995) discussed the implementation of a backward first-order LSE for the estimation of source of emission characteristics from concentrations. J. A. Pudykiewicz (1998) developed the adjoint operator of a Eulerian advection–diffusion model for similar applications. It turns out that the adjoint of the Eulerian advection–diffusion equation and of the equivalent Lagrangian random displacement model, Eq. (7), is simply the forward equation with the average or synoptic wind reversed. Diffusion and removal processes are treated the same as in forward mode.

An inverse version of MLDP0 has been developed and is used to support the operations of the Comprehensive Nuclear-Test-Ban Treaty (CTBT) Organization (WMO, 2010, updated 2012, Appendix I-6, Appendix II-9). The results of adjoint or inverse models are often referred to as Source Receptor Sensitivity (SRS) coefficients (Wotawa et al., 2003). Simply put, the SRS coefficients are a measure of the amount of air transported from a given region of the atmosphere (a possible source location) into the sampler where the concentrations are measured.

l *The Trajectory Model*

In some cases, however, one is simply interested in visualizing the tracks of a few large air parcels. A simple and fast trajectory calculation module was implemented for that specific purpose. Again, it is assumed that the identity of the air parcels is preserved as they move with the wind and that they are not affected by any other processes. The change in the position of a given air parcel is obtained by integrating its velocity in time:

$$\Delta \mathbf{r} = \int_{t_0}^{t_0+\Delta t} \mathbf{V}(\mathbf{r}, t) dt \tag{40}$$

where $\mathbf{V}(\mathbf{r}, t)$ represents the 3D wind velocity. The time discretization is carried out using a Runge-Kutta algorithm. Because of the fourth-order accuracy of this scheme, it is possible to use a large time step. Usually it is chosen as the time interval at which the 3D wind fields are provided—one to six hours. Because the resulting horizontal finite displacements can be relatively large, and they are calculated on the sphere, some care must be used in their estimation. Because of its very basic approach, it is difficult to objectively evaluate a trajectory model. Nevertheless, the CMC trajectory model has been used extensively over the years in various contexts (e.g., Mercier et al., 2009) and its usefulness amply demonstrated.

5 Validation

a *Validation of MLCD for Local Dispersion with the Gentilly SF_6 Tracer Experiment*

Most short-range dispersion tracer experiments are performed under ideal conditions (e.g., Project Prairie Grass; Barad, 1958) and often in controlled wind tunnel experiments (Legg, Raupach, & Coppin, 1986). The algorithms used in the short-range dispersion module MLCD have been well tested using data from such experiments (e.g., J. D. Wilson et al., 1993, 1981a).

A short-range tracer experiment was performed in September and October 1997 on the grounds of the Gentilly Nuclear Power Plant, on the east shore of the St. Lawrence River, with controlled releases of sulphur hexafluoride (SF_6). Details of the experiment are given in Davis, Johnston, Workman, and Chouhan (unpublished manuscript). The site is reasonably representative of the complex geometry usually found in large industrial compounds. The tracer gas was released from a stack on top of the service building of the power plant at a height of 37 m above ground. Average tracer concentrations at each sampler for the first four releases were

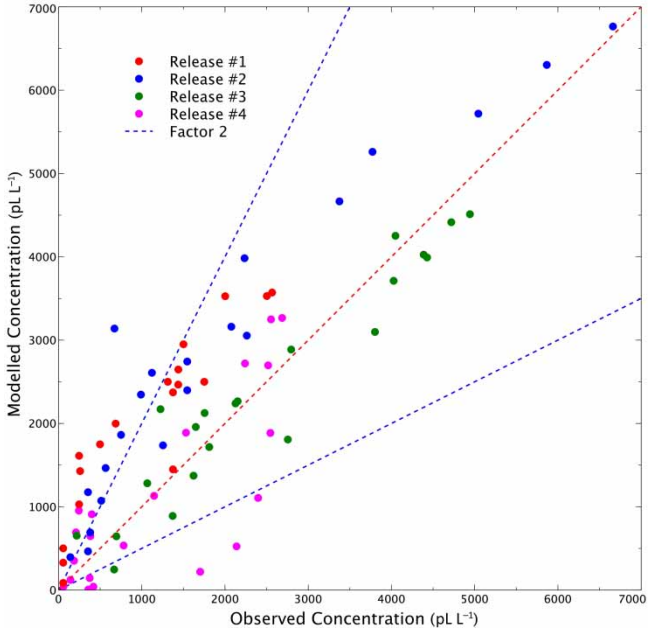

Fig. 1 Global scatter diagram: MLCD modelled versus observed volume mixing ratios. There are 81 data points. The Pearson linear correlation coefficient is 0.88.

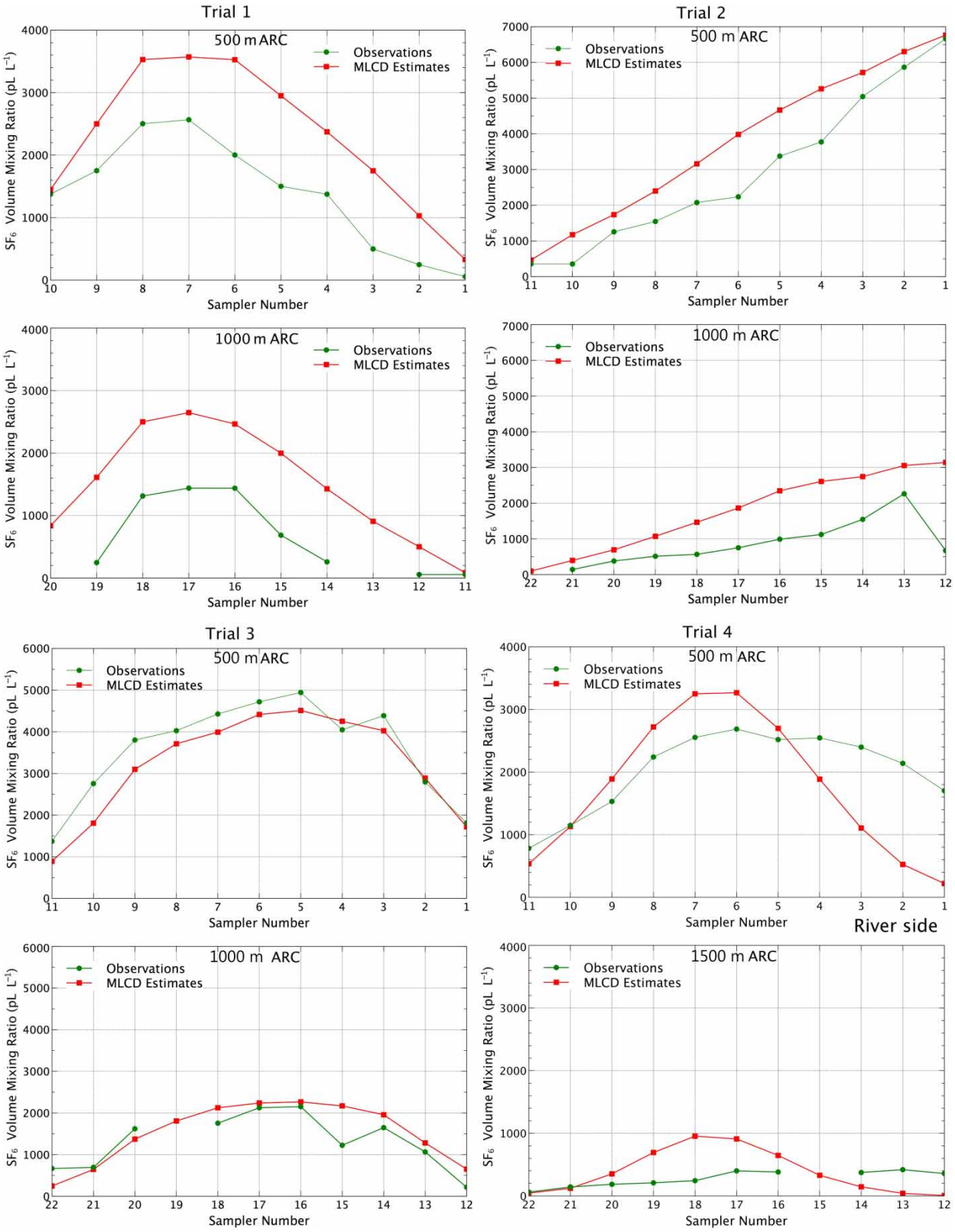

Fig. 2 Average observed and MLCD modelled concentrations for each release and arc. The sampler numbers increase from right to left in order to reflect their approximate east to west disposition, the plumes going generally from north to south. In trial 4 the wind was more or less along the St. Lawrence River.

TABLE 1. Some conditions during the SF_6 releases.

Release	Duration (s)	Release rate ($m^3\ s^{-1}$)	Average Monin-Obukhov length scale (m)	Estimated inversion height (m)
1	3600	1.67×10^{-4}	203	700
2	3180	5.34×10^{-4}	448	700
3	3600	2.94×10^{-4}	–943	700
4	3600	2.95×10^{-4}	–460	900

made available for the validation of MLCD. Table 1 shows the duration and the rates of the releases. For each release, the layout of the samplers was rearranged according to the mean wind direction. The samplers were placed on two arcs about 500 and 1000 m from the release, near the ground; 15-minute averages of wind speed and direction and of air temperature, measured routinely at 10, 37 and 48 m heights, were used as meteorological input to MLCD. The height of the boundary layer was estimated by Davis et al. (unpublished manuscript), and the Monin-Obukhov length scale L was evaluated from the tower measurements (see Appendix B).

Figure 1 shows a scatter diagram of the modelled versus measured average concentrations. In total 81 measurements were available, out of a possible 86; five were not available for technical reasons. The Pearson linear correlation coefficient for the total set is 0.88; 65% of the modelled concentrations are within a factor of two of the observations, and 87% within a factor of five.

Figure 2 allows a more direct comparison of the average modelled and observed concentrations at each sampler along the different arcs. The model is quite successful at positioning the axis of maximum concentrations and at depicting the lateral extent of the plume. The concentrations resulting from the modelling are somewhat overestimated for release #1. According to Table 1 the thermal stability was quite high, so a possible explanation could be that there was excess downward mixing in the modelled plume. Release #4 seems to show a somewhat different behaviour of the plume especially at 1000 m. For this case, the samplers were positioned on an axis more aligned with the shore of the St. Lawrence River. Even though the winds observed at the tower appear quite consistent with those reported at a meteorological station situated on the other side of the river (not shown here), it is suspected that local wind convergence induced by the roughness change between the land and water might have induced a pull of the plume towards the river, causing more lateral spread in the plume than the model could simulate.

b *Short-to Medium-Range Dispersion: An Accidental Release of Sulphur Trioxide Near Montréal, Canada*

Around 22:00 EDT 9 August 2004 (0200 UTC 10 August), about six tonnes of sulphur trioxide (SO_3) were accidentally released from a chemical factory in Salaberry-de-Valleyfield, about 50 km southwest of downtown Montréal. The incident triggered a real-time emergency response from the CMC. The SO_3 escaped through a chimney stack about 80 m high over approximately a period of 30 minutes. After entering the atmosphere, the SO_3 gases rapidly reacted with the ambient water vapour to form sulphate aerosols, resulting in a plume which reached the city of Montréal a few hours later. A fine mist was observed in downtown Montréal during the passage of the plume around midnight, and a significant increase in particulate matter concentrations ($PM_{2.5}$) was observed at some stations in the city's air quality monitoring network (Paquin & D'Amours, 2005). Because most of the sulphate aerosols produced in the atmosphere have a diameter smaller than 1.0 μm (Hazi, Heikkinen, & Cohen, 2003), it can be safely assumed that the sudden increase in particulate matter was the result of the SO_3 plume. The availability of these observational data provides an opportunity to evaluate the performance of the dispersion models.

The intermediate scale of the problem was somewhat problematic for the operational response. Using the local MLCD at first appeared to be inappropriate, mainly because of the uniform horizontal wind field assumption. On the other hand, it seemed that the spatial scale of the release was at the resolution limit of the available regional meteorological fields provided by NWP (15 km grid spacing). In the end, because the meteorological conditions were estimated to be fairly uniform in the horizontal over the domain of concern, it was decided to use MLCD for the initial response. Figure 3a shows the position of the plume estimated by MLCD 2.5 h after the start of the release, based on a prudent original estimate of 10 t for the release provided by emergency responders. The plume cuts off abruptly at the northeast end at the edge of the model domain. Figure 3b shows an MLDPmm simulation after the fact for the same time, using 6–12 h forecast meteorology from the CMC 15 km regional model in operation at the time, which would have been available for a real-time response, also using a revised release of 6 t provided later by plant authorities. In the MLDPmm configuration, particle trajectories were calculated with the first-order algorithm, during the first hour after their release, and with the zeroth-order algorithm afterwards.

Over the island of Montréal, the size and shape of the two modelled plumes are rather similar, but the slight shift in their trajectories is significant in terms of potential impacts. The MLDPmm plume sweeps right over the downtown area of the city, whereas the MLCD plume generally travels over the northern half of the island. Figure 4 shows time series of modelled SO_3 concentrations in comparison with observed $PM_{2.5}$ concentrations at two downtown air quality monitoring stations. The timing of the MLDPmm plume passage is very good. The MLCD plume arrives at the stations about 30 to 45 minutes early. Concentrations are lower than those of MLDPmm, reflecting the fact that the brunt of the MLCD plume skimmed by the two stations. Also, according to the MLCD simulation, stations AUT and RDP should have seen increased concentrations and that was not observed. There were no attempts to model the transformation of SO_3 into H_2SO_4 aerosols or to estimate the quantity of $PM_{2.5}$ that could result from the process, so a direct

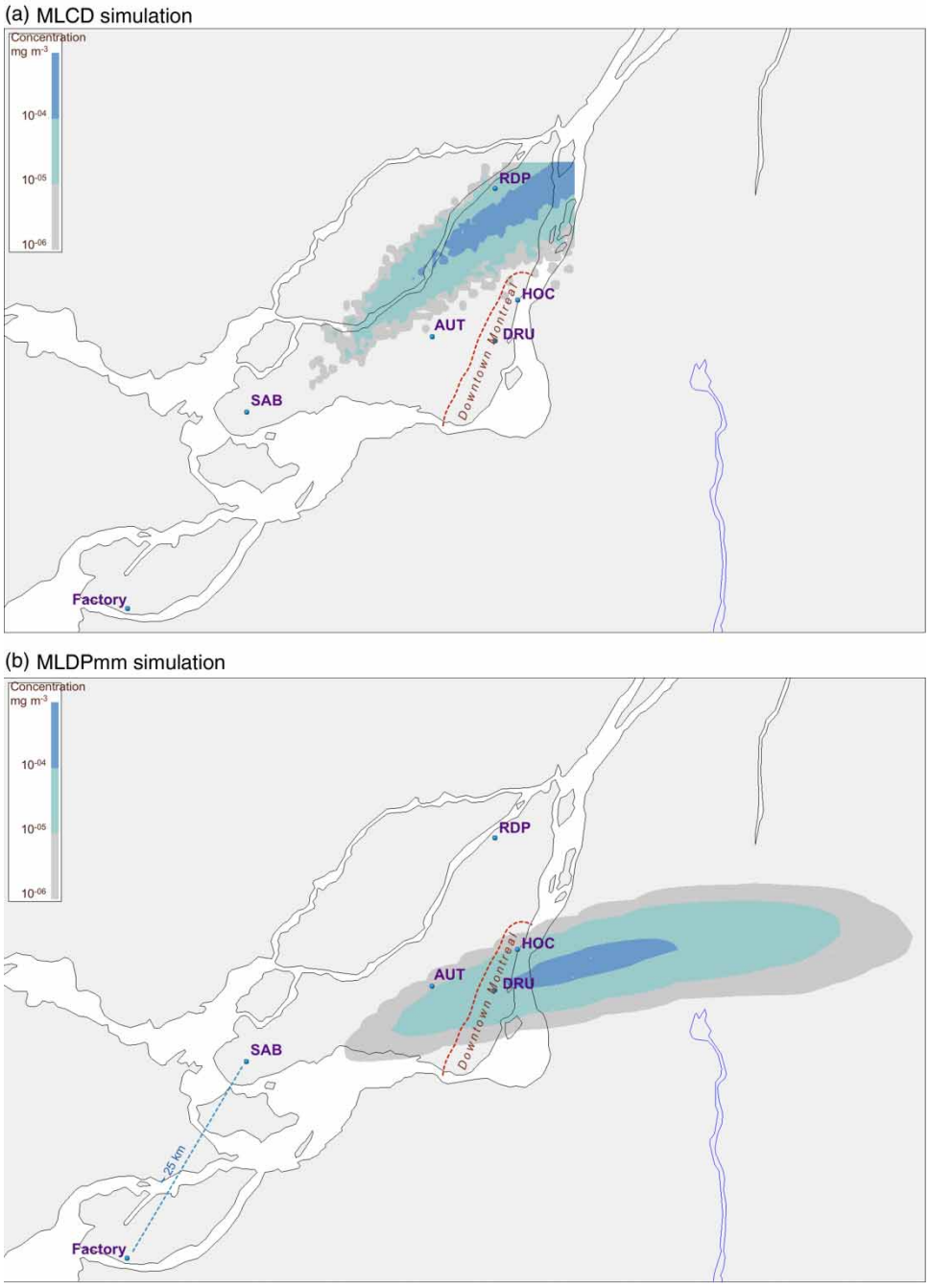

Fig. 3 Modelled surface concentrations at 00:30 EDT 10 August 2004 (0430 UTC 11 August 2014), 2.5 hours after the start of the release. The point labelled Factory shows the location of the SO_3 release. The other points show the location of the Montréal air quality monitoring stations. Only the downtown stations DRU and HOC reported $PM_{2.5}$ concentrations significantly above background levels. The distance between the Factory and SAB is ~25 km and between DRU and HOC about 5 km. The MLCD modelling domain is smaller than the map shown.

comparison is not possible. However, it is not unreasonable to assume that the $PM_{2.5}$ concentrations would be larger than the un-transformed SO_3 concentrations. Therefore, concentrations produced by the MLDPmm simulation appear quite reasonable. It also indicates that there is a real benefit to using the full time-varying 3D meteorology, despite the fact that conditions seemed fairly uniform in space and time during the few hours following the incident.

c *Continental Dispersion: The First Release of the European Tracer Experiment*

Details of the European Tracer Experiment (ETEX) can be found in Girardi et al. (1998). The first release, ETEX-1, took place on 23 October 1994. An inert perfluorocarbon tracer (PMCH) was released from a small chimney (4 m high) at a constant rate, over 12 hours, starting at 1600 UTC, in Monterfil in western France. A total of 340 kg of tracer

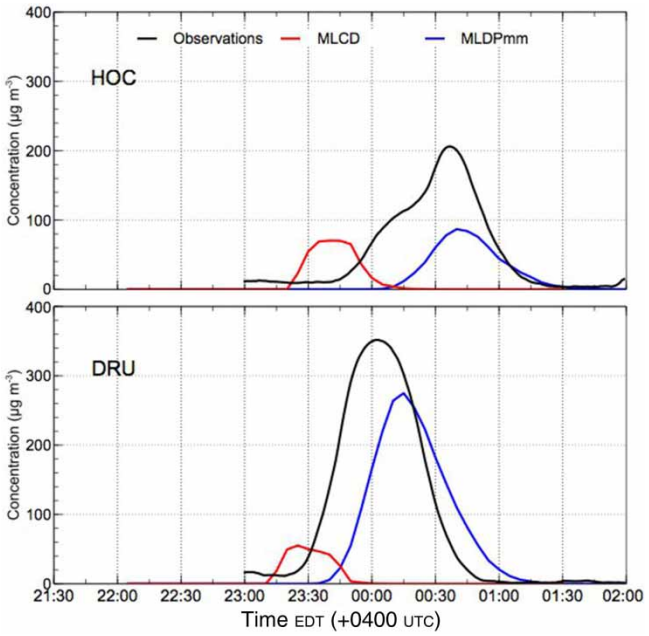

Fig. 4 Time series of modelled SO_3 and observed $PM_{2.5}$ concentrations at the two stations reporting concentrations above background levels.

TABLE 2. User-oriented measures of effectiveness for three configurations of MLDP applied for the ETEX first release. Results obtained by CANERM for ATMES II are also shown.

Model	Objective score function (OSF)	Figure of merit in space (FMS)	Fractional bias (FB)
MLDP0	0.436	0.530	–0.17
MLDP1	0.407	0.554	–0.13
MLDPmm	0.388	0.570	–0.06
202[a]	0.419	0.545	—
105[b]	0.451	0.514	—

[a]CANERM executed with CMC global meteorological analyses. Results from Warner et al. (2004), Table 2.
[b]CANERM executed with ECMWF meteorological analyses, also from Warner et al. (2004), Table 2.

was released and 3-hour average concentrations were measured at 168 sampling stations for up to 96 hours after the start of the release. Details of the observational data are given in Nodop, Connolly, and Girardi (1998).

ETEX-1 had two phases: a real-time phase in which participants had to respond with forecast wind fields, as if in a real accident, and the Atmospheric Transport Models Evaluation, II (ATMES II) in which participants ran their model with analyzed (diagnostic) meteorology, while having access to the measured concentration data. Results for the real-time response can be found in Graziani, Klug, and Mosca (1998) and a report on the model evaluation study in Mosca, Bianconi, Bellasio, Graziani, and Klug (1998). Warner, Platt, and Heagy (2004) later applied user-oriented measures of

TABLE 3. ^{133}Xe activity mean release rate for 12 March 0000 UTC to 15 March 1200 UTC.

Type	Release rate (Bq h^{-1})
Sidney Scaled SRS sum	2.4×10^{18}
Vancouver Island tracks	2.0×10^{18}
PNNL Scaled SRS	4.0×10^{17}
Stohl et al. (2012)	1.7×10^{17}

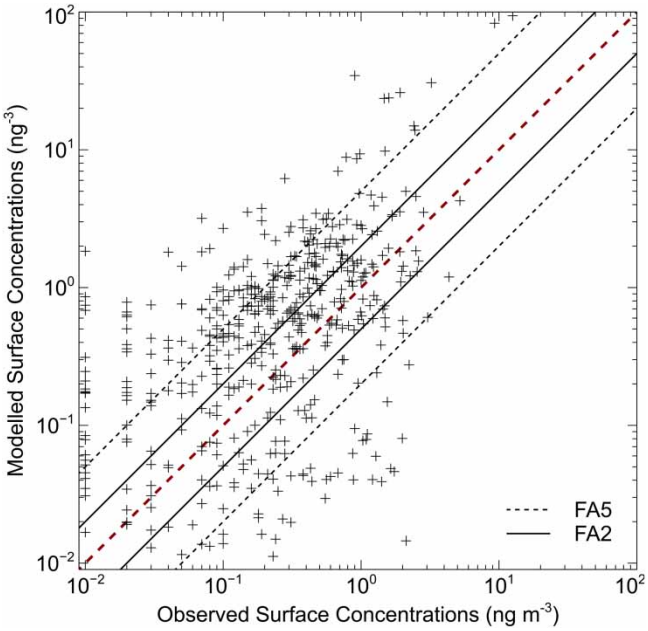

Fig. 5 ETEX global scatter diagram: MLDPmm versus observed concentrations. The FA2 and FA5 lines give the limits of the regions where concentrations are within a factor of two and a factor of five, respectively, of each other.

effectiveness (MOE) to the model results of the atmospheric transport model evaluation study ATMES II. According to Tables 2 and 3 of that study, the CMC simulations (models 105 and 202) using the Canadian Emergency Response Model (CANERM), a Eulerian dispersion model, in operation at the time, (D'Amours, 1998; J. Pudykiewicz, 1989) performed quite well.

The MLDP0, MLDP1, and MLDPmm simulations of the release used meteorological fields based on a sequence of short-term forecasts (3 and 6 hours) from the CMC NWP model, which was executed at 15 km grid spacing over a European domain specially for ETEX. These meteorological fields were produced for a study by D'Amours (1998). The dispersion simulations were executed up to 27 October 1200 UTC, a duration of 92 hours from the start of the release.

Table 2 shows three verification scores for a concentration threshold of 0.01 ng m^{-3}[†] based on the Warner et al. (2004) user-oriented objective MOEs. Calculation details are given in Appendix C. The objective scoring functions (OSF), the

[†]The lowest non-zero concentration available in the observation dataset.

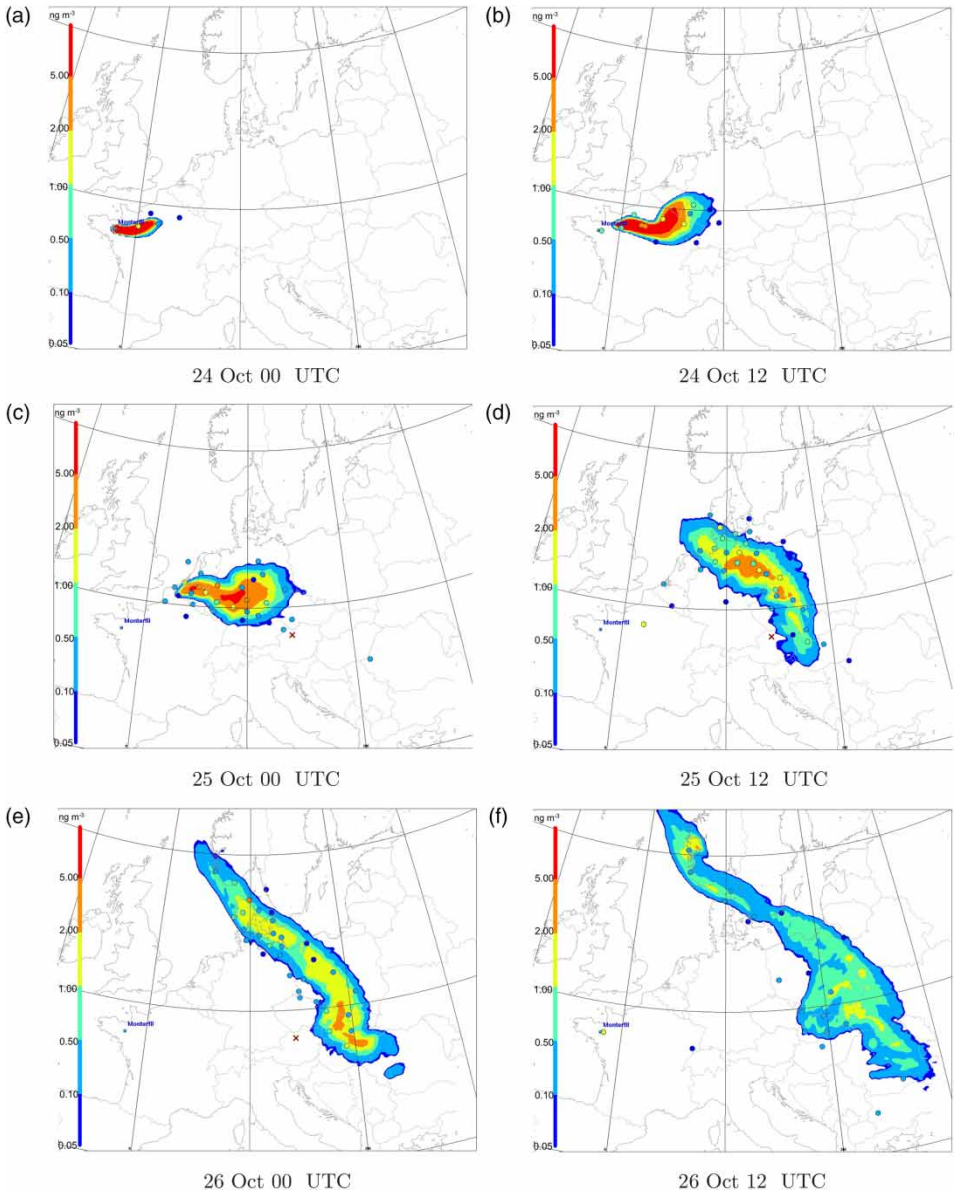

Fig. 6 MLDPmm 3-hour average surface concentrations for six different times. Corresponding 3-hour average observed concentrations are also plotted as coloured dots, using the same colour pattern. The × symbol, in dark red, on panels (c), (d), and (e) shows the approximate position of Austrian station A04 where only zero tracer concentrations were observed during the experiment.

figure of merit in space (FMS), and the fractional bias (FB) were calculated. The OSF is a measure of the distance between the perfect overlap and the actual results. The FMS gives the ratio of the overlapping stations having concentrations above a threshold of interest to the union of the stations where either the modelling or the observations show concentrations above that threshold. The target scores are OSF=0 and FMS=1. If FB=0 then the modelled and observed plumes are about the same "size," and a negative FB indicates a tendency of the model to overestimate the extent of the plume.

In Table 2, MLDP0 refers to the zeroth-order configuration of the transport model described in the first part of the paper; MLDP1 corresponds to the first-order configuration; MLDPmm corresponds to a mixed mode configuration in which the particle trajectories were calculated according to the first-order Langevin equation mode for the first hour after their release and afterwards, in zeroth-order mode, using a diffusion coefficient calculated as $\sigma_w^2 T_L$. For MLDP1 and MLDPmm, the variance of the turbulent wind components, σ_u^2, σ_v^2, and σ_w^2 was estimated by splitting the TKE provided by the NWP model simulations, as described in Section 4.2.1.

According to the MOE scores in Table 2, the Eulerian model based on CMC meteorological analyses produced better results than when executed with European Centre for

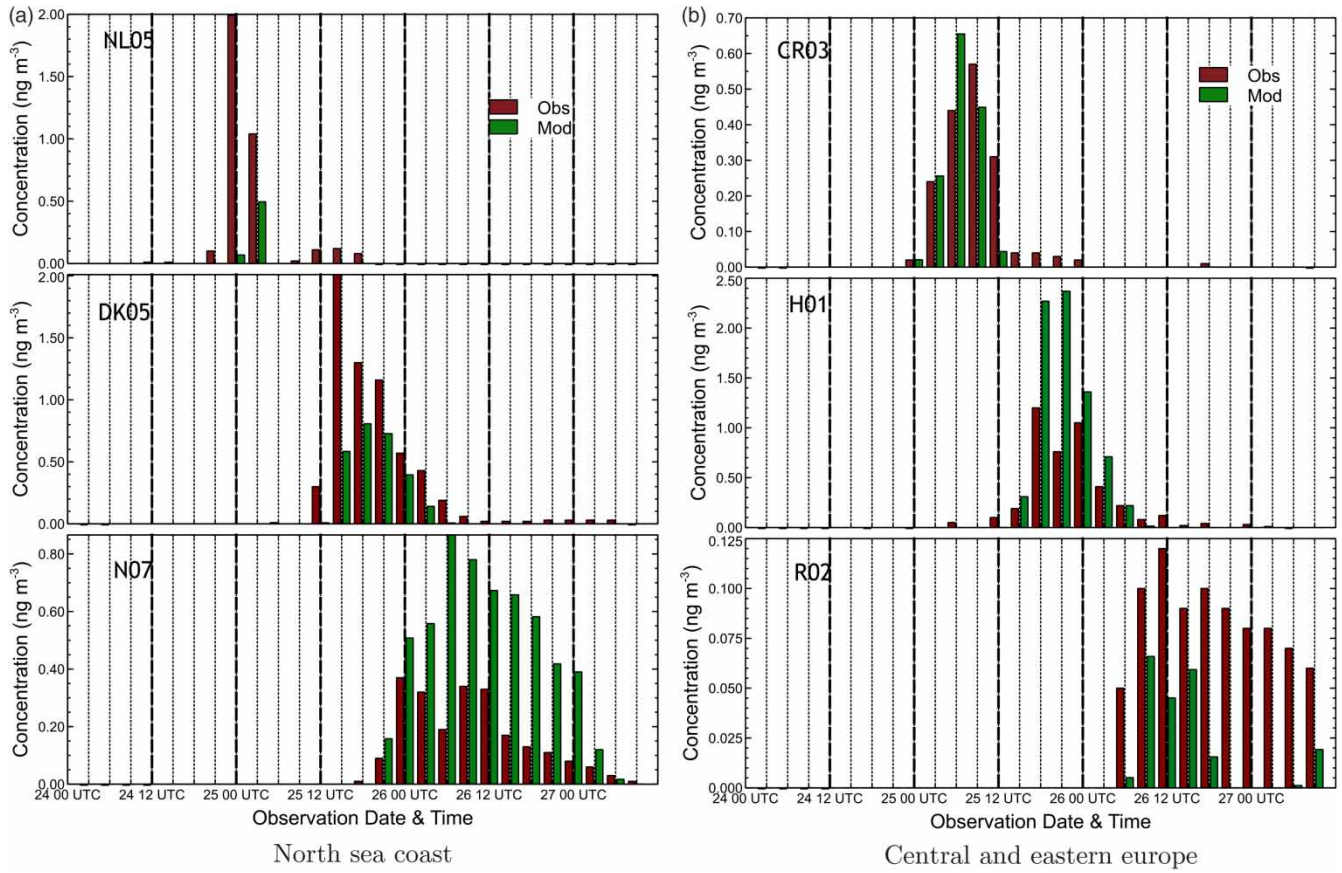

Fig. 7 Time series of measured and modelled surface concentrations at three stations near the North Sea coastline that experienced the passage of the ETEX plume tail end: NL05 (Vlissingen, The Netherlands), DK05 (Hvide Sande, Denmark), and N07 (Stavanger, Norway) and at three stations in central and eastern Europe: CR03 (Praha, Czech Republic), H01 (Budapest, Hungary), and R02 (Bucuresti, Romania). Note the different scales on the vertical axes.

Medium-range Weather Forecasts (ECMWF) meteorological data. The score of the zeroth-order Lagrangian MLDP0 is intermediate between models 202 and 105. The first-order Lagrangian MLDP1 produced better results than the CANERM and MLDP0. However, it is intriguing to note that the mixed mode Lagrangian MLDPmm produced the best results. The reasons for this have not been identified.

Figure 5 shows a scatter diagram of MLDPmm concentrations versus observed concentrations. A tendency to overestimate in-plume concentrations, also noted in CANERM in ATMES II, is still present. Figure 6 shows the evolution of the surface plume produced by the MLDPmm simulations with a plot of the corresponding observed station concentrations. Because the minimum detected concentration was 0.01 ng m^{-3}, only values above 0.05 ng m^{-3} are shown.

The general evolution of the plume is well depicted, including the deformation and stretching that takes place starting 25 October 0000 UTC. The model appears to underestimate the extreme tail end of the plume as it travels along the North Sea coastline, over the Netherlands and Denmark, while somewhat overestimating the portion travelling over central Europe. This can also be seen in some of the time series of the observed and modelled surface concentrations shown in Figs 7a and 7b. The timing of the passage of the plume is very well depicted, even at the extreme edges over Norway and Romania.

d *Global Scale Dispersion: Arrival of the Fukushima Plume on the North American Coast of the Northwestern Pacific*

The accidental release of radioactive substances from the Fukushima Daiichi Nuclear Power Plant, following the tsunami of 11 March 2011, provides a unique opportunity to test and validate dispersion models against observational data (Chino et al., 2011; Draxler et al., 2015; Draxler & Rolph, 2012; Terada, Katata, Chino, & Nagai, 2012). A low-level radioactive xenon (^{133}Xe) plume was detected with a high temporal resolution over Sidney, British Columbia, Canada. Radioactive cesium (^{137}Cs) was also observed but with much lower activity concentrations. Figure 8 shows a time series of the ^{133}Xe and of ^{137}Cs activity concentrations observed over Sidney. Measurements of ^{133}Xe were also taken with an airborne detector, at high spatial resolution, along the west coast of Vancouver Island (Sinclair et al., 2011). The plume was also observed in Richland, at the Pacific Northwest National Lab (PNNL), Washington State (Ian Hoffman, personal communication, 2011).

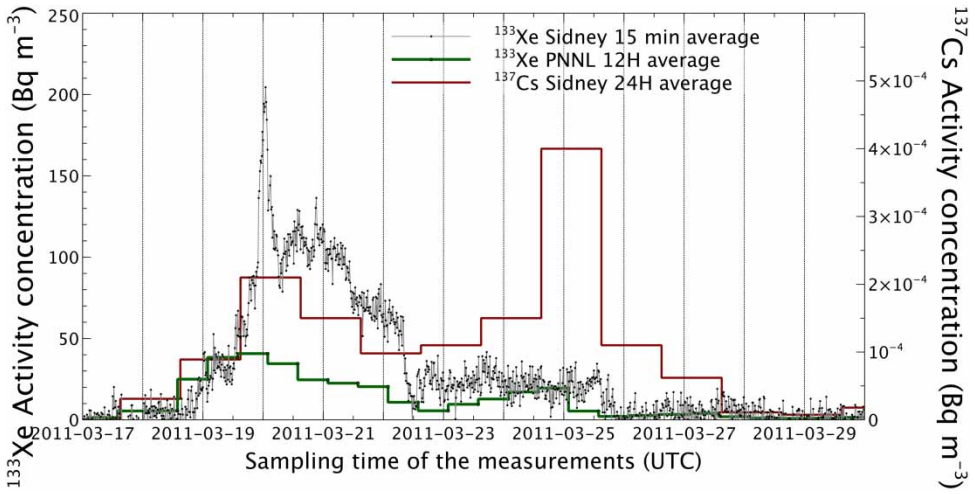

Fig. 8 Time series of ^{133}Xe and ^{137}Cs activity concentrations observed in Sidney, on Vancouver Island, and ^{133}Xe observed at PNNL, Washington State.

The amounts and timeline of the radioactive releases from Fukushima during the first days after the tsunami hit are still under investigation; however, several studies on the subject are available (e.g., Chino et al. 2011; Katata, Ota, Terada, Chino, and Nagai, 2012; Stohl et al., 2012). To investigate the effects of the uncertainties in the radioactive emissions, a series of ^{133}Xe dispersion simulations, based on releases of one unit per hour over six hours, were conducted for a few days starting 12 March 0000 UTC. The resulting air concentrations from such unit releases can be seen as a measure of the relative amount of air originating from the source location, taking into account the effect of radioactive decay. This is often known as the source-receptor sensitivity factor (SRS) (Wotawa et al., 2003), or source-receptor matrix (SRM) (Seibert & Frank, 2004), and also as the transfer coefficient matrix (TCM) (Draxler & Rolph, 2012).

According to news reports, the tsunami struck the power plant at 0630 UTC 11 March (Stohl et al., 2012; TEPCO, 2012), and radioactive releases could have started some 15 hours later. Figure 9 shows the Sidney SRS time series resulting from a sequence of 6-hour unit emissions, starting 12 March 0000 UTC. Interestingly, all SRS time series show rather similar patterns, although with different intensities. The Sidney location shows much reduced sensitivity to

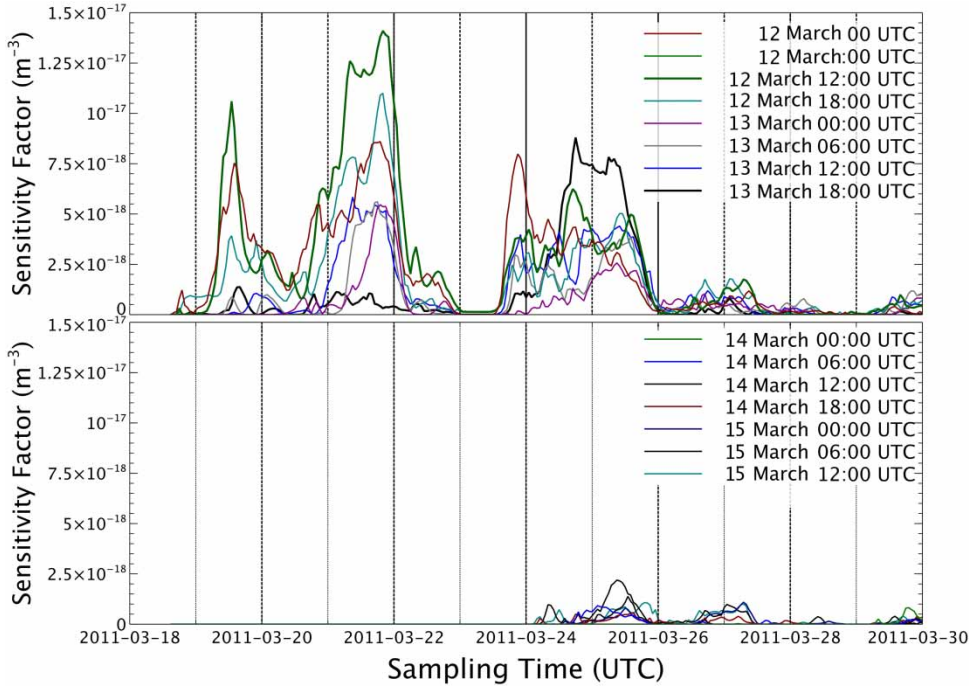

Fig. 9 SRS time series for Sidney, Vancouver Island, to 6-hour ^{133}Xe emissions (one unit) from Fukushima. (Top panel) 12 March 0000 UTC to 13 March 1800 UTC, (bottom panel) 14 March 0000 UTC to 15 March 1200 UTC. The location of Sidney can be seen in Fig. 13.

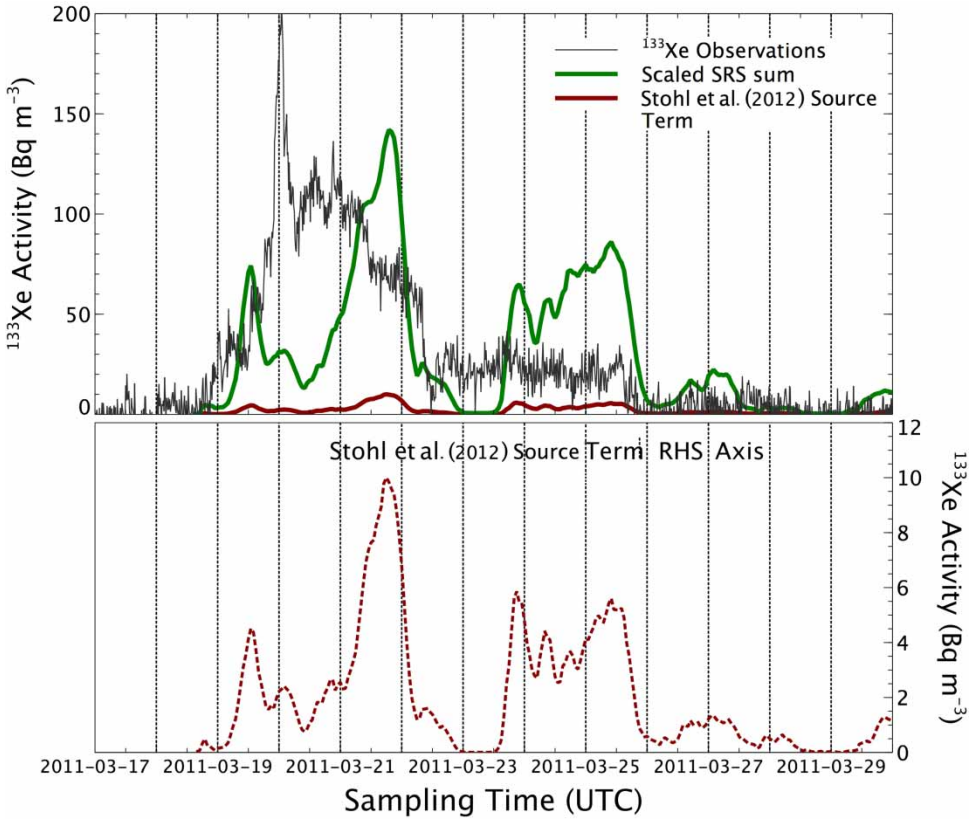

Fig. 10 Time series of modelled and observed ^{133}Xe for Sidney, on Vancouver Island. The scaled SRS sum implies a constant emission rate from 12 March 0000 UTC to 14 March 0000 UTC (see Table 3). The lower panel reproduces the concentrations obtained using the Stohl et al. (2012) source term, with a different axis, on the right-hand side, in order to show the details of the time series more clearly.

possible emissions from Fukushima occurring after 13 March (bottom panel of Fig. 9). These SRSs were combined and scaled into ^{133}Xe activity concentration as follows. Let $\mathbb{S}_i$ represent a given combination of SRSs for observation i, and $\overline{\mathbb{S}}$ the average of all $\mathbb{S}_i$, then:

$$\tilde{c}_i = \mathbb{S}_i \frac{\overline{c_{\text{obs}}}}{\overline{\mathbb{S}}}, \tag{41}$$

where $\tilde{c}_i$ is the modelled or scaled concentration for observation i and $\overline{c_{\text{obs}}}$ the average observed concentrations. There is an implicit source term resulting from the scaling and it will be discussed further below.

In the top panel of Fig. 10, one can see $\tilde{c}$ resulting from the simple summation of all scaled SRS time series (Scaled SRS sum), the green line. In general the model results give more sharp features than were observed. The time of the plume arrival, on 19 March, some seven days after the beginning of the release, is very well captured. There is a double peak in the first period of elevated activity, which was not observed, but the timing of the sharp decline at the end of the high activity period is also well captured. The modelling shows a

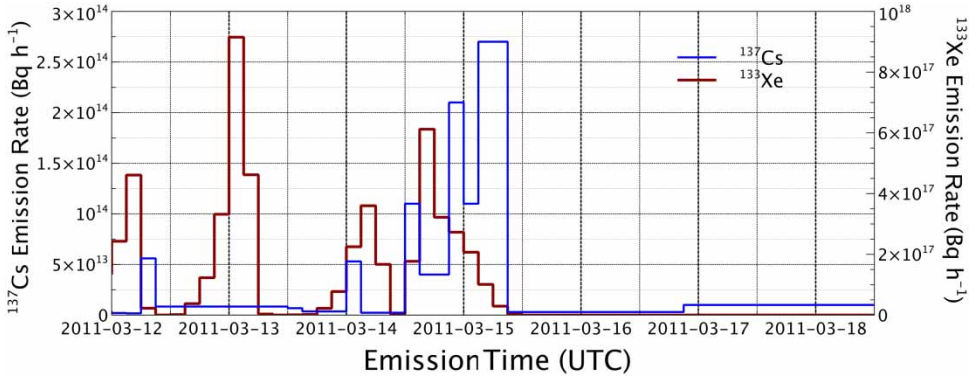

Fig. 11 ^{137}Cs and ^{133}Xe emission rates used for the MLDP simulations. These rates are based on Terada et al. (2012) and Stohl et al. (2012).

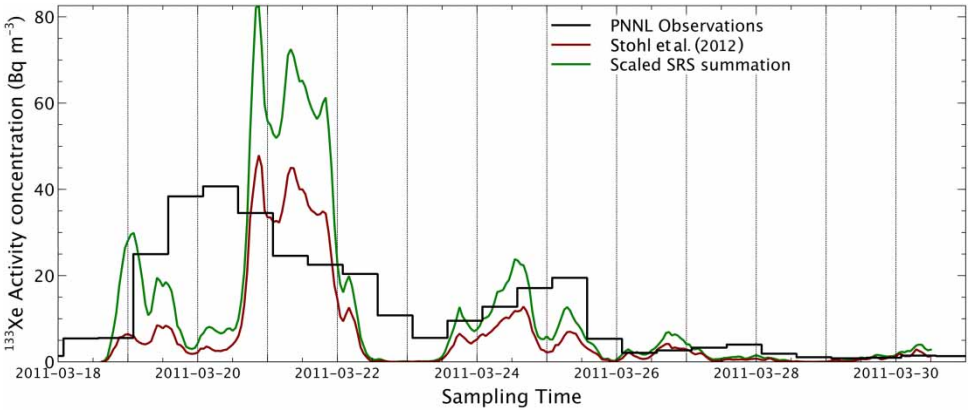

Fig. 12 Time series of modelled versus observed ^{133}Xe activity concentration, Richland, Washington State, shown as PNNL in Fig. 13.

second relatively intense peak, where a plateau of clearly above-background activity is seen. The observed timing of the return to background levels coincides quite well with the end of the second peak in the modelling. The application of the Stohl et al. (2012) source term, mapped into 6-hour average emission rates (dark red line Fig. 11), yields lower concentrations than were observed by about an order of magnitude. The bottom panel of Fig. 10 shows the model response to the Stohl et al. (2012) source term in more detail; the response pattern is very similar to that of a uniform release. This indicates that at long range the modelling results are more sensitive to the transport process than to the details of the release. Since Stohl et al. (2012) emission estimates are very credible, this suggests that MLDPmm underestimates concentrations in Sidney. Possible reasons for this are discussed later.

The SRS time series for Richland, Washington State (PNNL), scaled into ^{133}Xe activity concentration $\tilde{c}$, in the same manner as for Sidney, are shown in Fig. 12, along with observations. The patterns of the model results for PNNL are very similar to those for Sidney. The Stohl et al. (2012) source term was also applied to the modelled SRS (dark red line). The resulting concentrations are much closer to the observations than with Sidney, and, interestingly, the observed concentrations are lower than those seen in Sidney.

In Fig. 13, the ^{133}Xe activity concentration measured by Sinclair et al. (2011) along the west coast of Vancouver Island, on 20 March, between 1800 UTC and 1900 UTC (black line with error bars), can be compared with the scaled model SRSs (red line) for the same observation points at the same time. The SRSs from the 6-hour emission runs were combined in the same manner as for Sidney and were also scaled into activity concentrations. At first glance, there does not appear to be much correlation between the modelled and the observed values; indeed, the linear correlation coefficient is 0.13. However, an inspection of the lagged cross-correlation (not shown) shows a maximum of about 0.8 at a lag of about 50 km. The dashed green line in Fig. 13 displays the model results shifted southeastward by about 50 km. The correspondence with the observations is now very good, indicating that the model depicts a real feature but with a slight displacement error.

Figure 14 illustrates a possible explanation: after being released from Fukushima, the ^{133}Xe plume becomes stretched

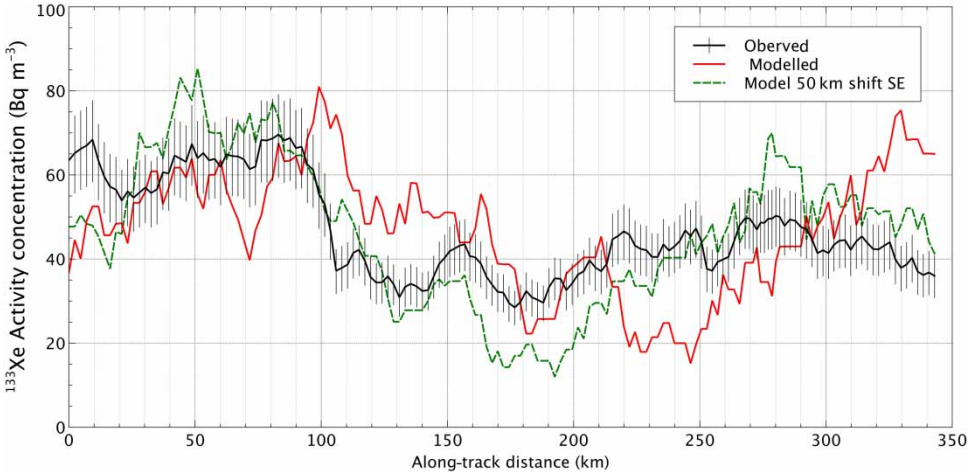

Fig. 13 Modelled (see text) and observed ^{133}Xe activity concentration along a track on the west coast of Vancouver Island. The track location can be seen on the map in Fig. 13.

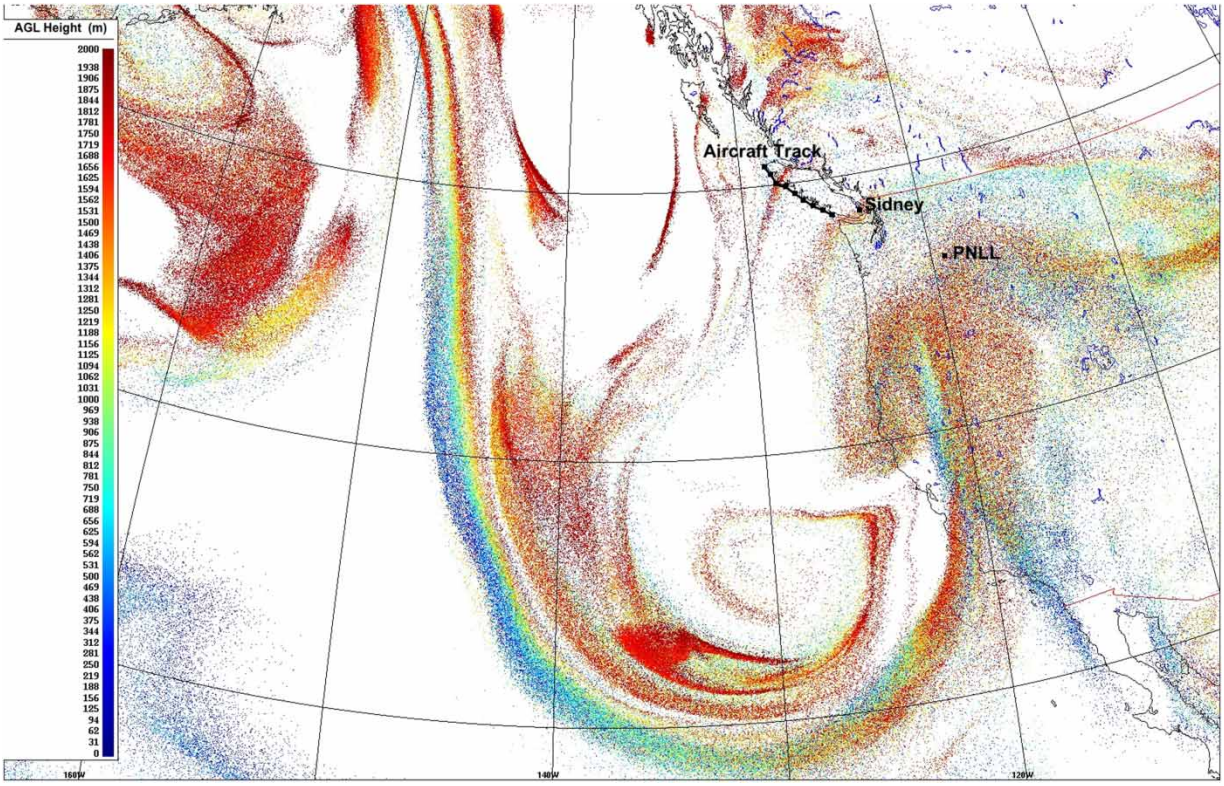

Fig. 14 Position of model particles 20 March 1800 UTC resulting from a continuous emission from Fukushima from 12 March 0000 UTC to 13 March 0000 UTC. Only particles in the lower 2000 m layer are shown. The aircraft tracked from SE to NW over a distance of about 350 km.

into relatively thin filaments around a developing low pressure system moving across the Pacific Ocean. These filaments seem to keep their identity because of reduced mixing when travelling over cold Pacific waters, and apparently it is their passage that results in the sharp features observed on Vancouver Island and in Richland.

Table 3 shows the different *implied* ^{133}Xe source terms in the scaling used for Figs 10 to 12, as well as the Stohl et al. (2012) source term, for 12 March 0000 UTC to 15 March 1200 UTC. The agreement between the estimate for PNNL and Stohl et al. (2012) is quite good, but there is an order of magnitude difference with those for Vancouver Island.

Figure 14 shows that the particle plume became quite mixed over Richland, after moving inland. There is not as much mixing near Vancouver Island, so a possible explanation would be that, although the model is able to simulate the sharp features associated with the filamenting, the model filaments are still not dense enough near the British Columbia

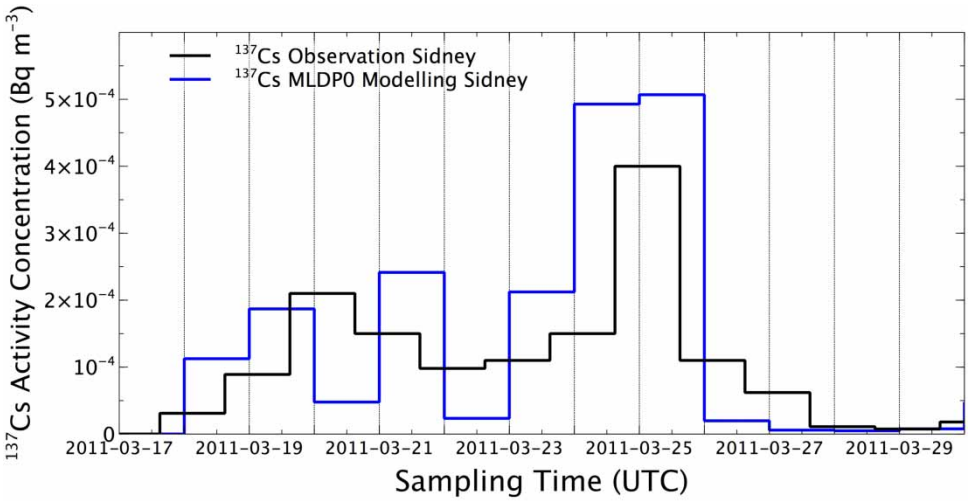

Fig. 15 Time series of modelled and observed ^{137}Cs for Sidney, Vancouver Island. The emission rates used are those of Terada et al. (2012) shown in Fig. 11.

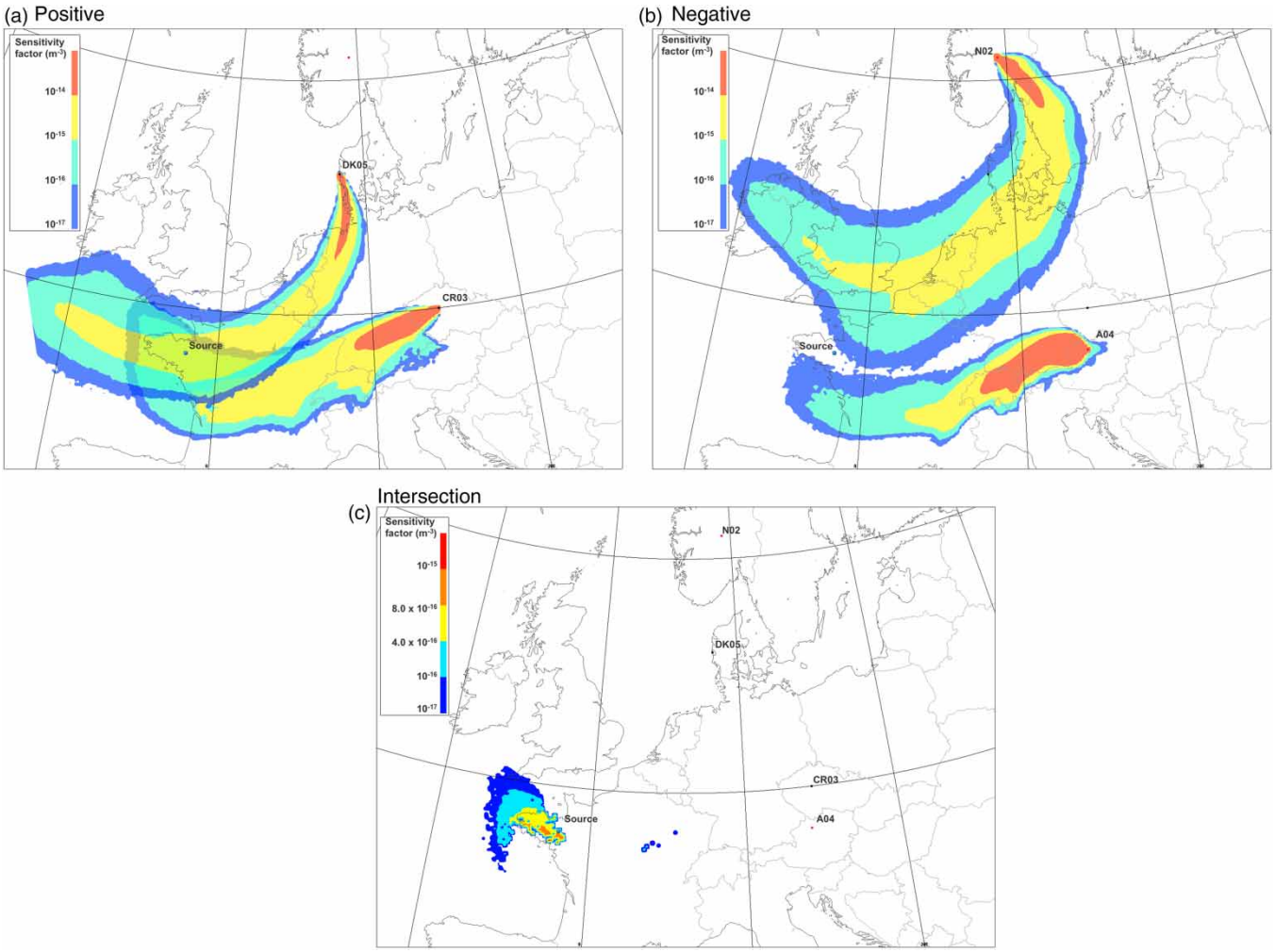

Fig. 16 Fields of Regard (FOR) for two stations that (a) clearly saw above-background tracer concentrations and (b) did not measure any tracer at a given time; (c) shows the average FOR in the region where the two plumes shown in (a) overlap, excluding any area where the plumes in (b) are seen. The observation time for CR03 is 25 October 0600 UTC and for DK05, 25 October 1800 UTC. For A04 the observation time is 25 October 0600 UTC and for N02, 26 October 1800 UTC. All inverse simulations end 23 October 1500 UTC.

coast resulting in an underestimation of the in-plume concentration. In other words, the model tends to dilute the dense filaments a little too soon, before they hit the coastal regions.

Figure 15 shows results of a simulation from MLDP0 for ^{137}Cs using the Terada et al. (2012) source term shown in Fig. 14. There is a reasonable amount of similarity between the modelled ^{137}Cs time series and that of ^{133}Xe. There is a double peak associated with the first activity period, between 19 and 22 March. There is also a second peak, between 23 and 27 March, which correlates well with the observed second period of elevated activity. Interestingly, aside from a small spike around 1200 UTC 12 March, the strongest emissions occur between 1200 UTC 14 March and 1200 UTC 15 March. Even though the SRSs shown in Fig. 9 are for ^{133}Xe, they are an indication that the second ^{137}Cs plume seen in Sidney on 24–25 March, was the result of the elevated emissions on 14–15 March, whereas the first plume observed on 19–20 March would have resulted from the much smaller emissions on 12 March. One could wonder why MLDP0 results are in fairly good agreement with ^{137}Cs observations in Sidney when MLDPmm underestimates ^{133}Xe at the same location. Results of ^{133}Xe simulations with MLDP0 (not shown) do not underestimate the concentrations in Sidney as much as MLDPmm does; however, those at PNNL are overestimated. The reasons for this were not investigated in depth, but appear to be related to the "lid" condition at the top of the boundary layer imposed on MLDP0 (Section 4.6).

e *Inverse Modelling with ETEX*

Results from inverse modelling can only be validated indirectly. A good measure would be the usefulness of the simulations in estimating the characteristics of a possible source of emission of a tracer, given a set of concentration measurements. Yee, Lien, Keats, and D'Amours (2008) used results from MLDP0, executed in inverse mode for the

ETEX-1 case, in an illustration of the Bayesian method for source reconstruction, which demonstrated the model capabilities. The observation dataset of ETEX-1 is extensive as was seen earlier in Section 5.3, but Yee et al. (2008) used a much smaller subset for their study, 35 measurements taken at 10 sampling sites.

Figure 16a shows what has been described as fields of regard (FOR) for two ETEX observing sites that measured well-above background tracer concentrations. Figure 16b shows FORs from two stations that measured zero concentrations. Here a FOR is the time average surface SRS field generated by a unit release from the observation site at the time when the measurement was made. A FOR delineates the region which is "sensed" by the sampler, regardless of the time at which that sensing would have occurred at any given point in the region. Assuming that the measurements are the result of a release from the same source, then the source should be in the region sensed by both samplers (i.e., where the FORs overlap) as illustrated by Fig. 16a. When observations are scarce, a zero concentration observation can be very useful. In that case, the possible source should not be in any part of the areas covered by the FORs resulting from those observations (Fig. 16b). Consideration of both types of FORs helps narrow the bounds of the possible location domain of the source. In Fig. 16c, the overlap of CR03 and DK05 FORs is obtained by taking the geometrical mean of the two fields. This area is then reduced by excluding regions where FORs from A04 or N02 are above the 10^{-18} threshold, and this is where the ETEX source is found. It should be noted that the intensity of the average SRS field within the limited area is by no means a measure of the source location probability. If no other information was available, it could only be concluded that the source is most likely to be found anywhere within that area.

The case of Austrian station A04 is quite interesting because none of the released tracer was observed there. Nevertheless, according to Fig. 6, the tracer plume appears to have moved around the station (indicated by the × symbol in dark red) for several hours during its complex stretching motion. The capacity of the models to reproduce zero concentrations can be quite important but was not assessed in the ATMES phase of ETEX (Mosca, Graziani, Klug, Bellasio, & Bianconi, 1998).

6 Conclusion

The Lagrangian transport and dispersion models in operation at CMC have been presented. These models are used for several types of environmental emergency responses, covering spatial scales from the very local, to regional or a few kilometres, to global. The theoretical bases of the models were discussed, and the main algorithms used in their implementation described. The performance of the models was evaluated with data from real cases of atmospheric spills of pollutants, confirming their usefulness. The dispersion models are continuously being validated and improved. Among other things, there are plans to improve the particle release modules to provide better simulations of explosive releases and heavy gas emissions. Work towards the implementation of a 3D Lagrangian scheme, coupled with complex urban flow fields is also taking place. Investigations of a source reconstruction algorithm for operational implementation are proceeding. The construction of a validation database using the low-level xenon emissions from the medical isotope production facility at Chalk River and measurements from the Health Canada monitoring network is expected to start soon.

Acknowledgements

The authors would like to thank Sohan Chouchan and Atomic Energy of Canada Limited for making available the Gentilly Tracer Experiment Data. Laurel Sinclair, of the Geological Survey of Canada is gratefully acknowledged for providing the British Columbia west coast aerial radioxenon concentration measurements. Ian Hofman and Kurt Ungar of the Radiation Protection Bureau, Health Canada, kindly provided the Sidney and PNNL ^{133}Xe and ^{137}Cs concentration data. Graphs were produced using the free software "Veuz" (http://home.gna.org/veusz/). Charts were produced using the CMC software SPI. Finally the authors would like to thank the anonymous reviewers for their useful and pertinent comments.

Appendix A: Concentration calculations

LSMs yield particle trajectories. A 3D concentration field, $c(\mathbf{r}, t)$, is obtained by estimating the conditional probability distribution of the particles in time and space:

$$c(\mathbf{r}, t) = \int_{-\infty}^{t} \int_{V} S(\mathbf{r}_0, t_0) p(\mathbf{r}, t|\mathbf{r}_0, t_0)\, d\mathbf{r}_0\, dt_0 \qquad \text{(A1)}$$

where $S(\mathbf{r}_0, t_0)$ is the source function, V is the 3D domain where the source is defined, and $p(\mathbf{r}, t|\mathbf{r}_0, t_0)$ the conditional probability that a particle is found at point $(\mathbf{r}, t)$, given that it was at point $(\mathbf{r}_0, t_0)$ (Sawford, 1985). In practice, particles are emitted at specific points in time and space, within the source volume, in a discrete fashion. For a single particle, the source function can be seen as a Dirac delta function, centred on the point where the particle was released. The particle concentration then becomes the conditional probability density function itself:

$$S(\mathbf{r}_0, t_0) = \delta(\mathbf{r}_0 - \mathbf{r}_p, t_0 - t_p) \qquad \text{(A2)}$$

$$\begin{aligned} c(\mathbf{r}, t) &= \int_{-\infty}^{t} \int_{V} \delta(\mathbf{r}_0 - \mathbf{r}_p, t_0 - t_p) p(\mathbf{r}, t|\mathbf{r}_0, t_0)\, d\mathbf{r}_0\, dt_0 \\ &= p(\mathbf{r}, t|\mathbf{r}_p, t_p)\,. \end{aligned} \qquad \text{(A3)}$$

If N particles are emitted with a mass m_p, from a set of points $(\mathbf{r}_p, t_p)$, then the resulting particle mass concentration is:

$$c(\mathbf{r}, t) = \sum_{p=1}^{N} m_p(\mathbf{r}, t) p(\mathbf{r}, t|\mathbf{r}_p, t_p). \qquad \text{(A4)}$$

Here the tracer "mass" m_p is a qualifier, or tag, characterizing the fluid element with which it is associated. If one assumes that the number of particles used in a simulation is sufficiently large such that their distribution in space at a given time is an adequate representation of the conditional probability distribution, then an estimation of this distribution can be obtained by counting the number of particles in each of the cells of a 3D array covering the domain of interest. The concentration at point $\mathbf{r}$ is simply:

$$c(\mathbf{r}, t) = \frac{1}{\delta V_s} \sum_{p \epsilon \delta V_s} m_p(\mathbf{r}, t), \tag{A5}$$

where δV_s is the volume of the cell centred on $\mathbf{r}$.

Other methods have been proposed essentially based on Eq. (A1). Indeed, the validity of this equation is not restricted to source-receptor relationships but can also form the basis of estimating the probability of a particle being at position $(\mathbf{r}, t)$ given that one is found at position $(\mathbf{r}_p, t_p)$. The problem is in the estimation of the functional form $p(\mathbf{r}, t|\mathbf{r}_p, t_p)$. Those functions are generally referred to as density kernels. Various formulations have been proposed (de Haan, 1999), and those all have a certain degree of arbitrariness.

Appendix B: Evaluation of the Monin-Obukhov length scale *L*

Following Eq. (13) in Delage (1997):

$$\frac{z}{L} = \frac{\phi_m^2}{\phi_H} \mathrm{Ri}, \tag{B1}$$

where ϕ_m and ϕ_H are the well-known universal functions for momentum and heat fluxes, respectively. These are normally written in terms of z/L, where z is the height above ground and L is the Monin-Obukhov length scale, an important scaling parameter for the surface layer. Delage (1997) reformulates the functions in terms of the Richardson number, a formulation used in CMC's GEM model (Mailhot et al., 1998).

For the unstable case, $\mathrm{Ri_{sl}} < 0$:

$$\phi_m^2 = \frac{\phi_H}{\beta} = (1 + 40\mathrm{Ri_{sl}})^{-1/3}, \tag{B2}$$

and for $\mathrm{Ri_{sl}} > 0$:

$$\phi_m = \frac{\phi_H}{\beta} = (1 + 12\mathrm{Ri_{sl}}), \tag{B3}$$

where $\beta = 0.85$, and $\mathrm{Ri_{sl}}$ is the gradient Richardson number evaluated at height z_{sl} within the surface layer.

The surface layer is usually assumed to be about 10% of the boundary layer. The vertical profiles of wind and temperature above the G2 meteorological tower were not available for our own evaluation of the boundary layer depth; however, it was estimated at around 700 m for trials 1 to 3 and around 900 m for trial 4 by scientists from Atomic Energy of Canada Ltd. We assumed that the tower data would be representative of the surface layer.

The Monin-Obukhov stability parameter $1/L$ can be evaluated as follows:

$$\frac{1}{L} = \frac{\mathrm{Ri_{sl}}}{z_{\mathrm{sl}}\beta} \qquad \mathrm{Ri_{sl}} < 0 \tag{B4}$$

$$\frac{1}{L} = \frac{\mathrm{Ri_{sl}}}{z_{\mathrm{sl}}} \frac{\phi_H}{\beta^2} = \frac{\mathrm{Ri_{sl}}}{z_{\mathrm{sl}}\beta}(1 + 12\mathrm{Ri_{sl}}) \qquad \mathrm{Ri_{sl}} > 0\,. \tag{B5}$$

For our purposes, $\mathrm{Ri_{sl}}$ was approximated by calculating differences between the 10 m and 47 m levels assuming they were representative of the gradient at the 37 m level.

$$\mathrm{Ri_{sl}} \approx \frac{g}{\theta} \frac{\Delta\theta \Delta z}{\left|\Delta \mathbf{U}^2\right|}\,. \tag{B6}$$

The potential temperature θ was approximated by $T + \gamma z$, γ being the dry adiabatic lapse rate, and T is expressed in Kelvin. Because, in principle, there is no wind direction change, in the vertical in the surface layer, and in fact there was not much observed, $\left|\Delta \mathbf{U}^2\right|$ was simply approximated by the square of the wind velocity differences between $z_{10\mathrm{m}}$ and $z_{47\mathrm{m}}$.

Appendix C: MOE scores

Adopting the Warner et al. (2004) convention,

$$x = \frac{N_{\mathrm{ov}}}{N_{\mathrm{obs}}} \quad \text{and} \quad y = \frac{N_{\mathrm{ov}}}{N_{\mathrm{mod}}}\,, \tag{C1}$$

where N_{ov} is the overlap (i.e., the number of stations for which both the modelling and observations show concentrations above a given threshold), N_{obs} is the total number of stations for which concentrations above the threshold are observed, and N_{mod} is the total number of stations for which the modelling yields concentrations above the threshold. The objective scoring function (OSF) is calculated as follows:

$$\mathrm{OSF} = \sqrt{(1-x)^2 + (1-y)^2}\,. \tag{C2}$$

The figure of merit in space (FMS) is calculated as follows:

$$\mathrm{FMS} = \frac{xy}{x + y - xy}. \tag{C3}$$

In this framework, the fractional bias (FB) is given by:

$$\mathrm{FB} = \frac{2(x-y)}{x+y}\,. \tag{C4}$$

References

Barad, M. (Ed.). (1958). *Project prairie grass, a field program in diffusion*. (Vol. 1) (No. 59). Air Force Cambridge Research Center.

Bécker, A., Wotawa, G., Geer, L.-E. D., Seibert, P., Draxler, R. R., Sloan, C., … Chen, P. (2007). Global backtracking of anthropogenic radionuclides by

means of a receptor oriented ensemble dispersion modelling system in support of Nuclear-Test-Ban Treaty verification. *Atmospheric Environment*, *41*(21), 4520–4534. doi:10.1016/j.atmosenv.2006.12.048

Bélair, S., Mailhot, J., Strapp, J. W., & MacPherson, J. I. (1999). An examination of local versus nonlocal aspects of a TKE-based boundary layer scheme in clear convective conditions. *Journal of Applied Meteorology*, *38*(10), 1499–1518. doi: 10.1175/1520-0450(1999)038<1499:AEOLVN>2.0.CO;2

Boughton, B. A., Delaurentis, J. M., & Dunn, W. E. (1987). A stochastic model of particle dispersion in the atmosphere. *Boundary-Layer Meteorology*, *40*(1), 147–163. doi:10.1007/BF00140073

Businger, J. A., Wyngaard, J. C., Izumi, Y., & Bradley, E. F. (1971). Flux-profile relationships in the atmospheric surface layer. *Journal of the Atmospheric Sciences*, *28*(2), 181–189. doi: 10.1175/1520-0469(1971)028<0181:FPRITA>2.0.CO;2

Chino, M., Nakayama, H., Nagai, H., Terada, H., Katata, G., & Yamazawa, H. (2011). Preliminary estimation of release amounts of ^{131}I and ^{137}Cs accidentally discharged from the Fukushima Daiichi nuclear power plant into the atmosphere. *Journal of Nuclear Science and Technology*, *48*(7), 1129–1134. doi:10.1080/18811248.2011.9711799

Canadian Meteorological Centre (CMC). 2013a. *Improvements to the Global Deterministic Prediction System (from version 2.2.2 to 3.0.0), and related changes to the regional deterministic prediction system (from version 3.0.0 to 3.1.0)* (Tech. Rep.). Canadian Meteorological Centre. Retrieved from http://collaboration.cmc.ec.gc.ca/cmc/CMOI/productguide/docs/lib/op systems/docopchanges/technote gdps300 20130213 e.pdf

Canadian Meteorological Centre (CMC). 2013b. *Improvements to the Regional Deterministic Prediction system (RDPS)* (Tech. Rep.). Canadian Meteorological Centre. Retrieved from http://collaboration.cmc.ec.gc.ca/cmc/CMOI/productguide/docs/lib/opsystems/docopchanges/technoterdps30020121003e.pdf

Canadian Meteorological Centre (CMC). 2011. *The Experimental High Resolution Deterministic Prediction System* (Tech. Rep.). Canadian Meteorological Centre. Retrieved from http://collaboration.cmc.ec.gc.ca/cmc/CMOI/productguide/docs/lib/opsystems/docopchanges/technotehrdps20111201e.pdf

Colette, A., Menut, L., Haeffelin, M., & Morille, Y. (2008). Impact of the transport of aerosols from the free troposphere towards the boundary layer on the air quality in the Paris area. *Atmospheric Environment*, *42*(2), 390–402. doi:10.1016/j.atmosenv.2007.09.044

Crum, T. D., & Stull, R. B. (1987). Field measurements of the amount of surface layer air versus height in the entrainment zone. *Journal of the Atmospheric Sciences*, *44*(19), 2743–2753. doi:10.1175/1520-0469(1987)044<2743:FMOTAO>2.0.CO;2

D'Amours, R. (1998). Modeling the ETEX plume dispersion with the Canadian emergency response model. *Atmospheric Environment*, *32*(24), 4335–4341. doi:10.1016/S1352-2310(98)00182-4

D'Amours, R., Malo, A., Servranckx, R., Bensimon, D., Trudel, S., & Gauthier-Bilodeau, J.- P. (2010). Application of the atmospheric Lagrangian particle dispersion model MLDP0 to the 2008 eruptions of Okmok and Kasatochi volcanoes. *J. Geophys. Res.*, *115*. doi:10.1029/2009JD013602

D'Amours, R., Mintz, R., Mooney, C., & Wiens, B. J. (2013). A modeling assessment of the origin of beryllium-7 and ozone in the Canadian Rocky Mountains. *Journal of Geophysical Research: Atmospheres*, *118*(17), 10,125–10,138. doi:10.1002/jgrd.50761

Delage, Y. (1988). A parameterization of the stable atmospheric boundary layer. *Boundary-Layer Meteorology*, *43*(4), 365–381. doi:10.1007/BF00121713

Delage, Y. (1997). Parameterising sub-grid scale vertical transport in atmospheric models under statically stable conditions. *Boundary-Layer Meteorology*, *82*(1), 23–48. doi:10.1023/A:1000132524077

Draxler, R., Arnold, D., Chino, M., Galmarini, S., Hort, M., Jones, A., … Wotawa, G. (2015). World Meteorological Organization's model simulations of the radionuclide dispersion and deposition from the Fukushima Daiichi nuclear power plant accident. *Journal of Environmental Radioactivity*, *139*, 172–184. doi:10.1016/j.jenvrad.2013.09.014

Draxler, R. R., & Rolph, G. D. (2012). Evaluation of the Transfer Coefficient Matrix (TCM) approach to model the atmospheric radionuclide air concentrations from Fukushima. *Journal of Geophysical Research: Atmospheres*, *117*(D5). doi:10.1029/2011JD017205

Durant, A. J., & Rose, W. I. (2009). Sedimentological constraints on hydrometeor-enhanced particle deposition: 1992 eruptions of Crater Peak, Alaska. *Journal of Volcanology and Geothermal Research*, *186*(1-2), 40–59. doi:10.1016/j.jvolgeores.2009.02.004

Durbin, P. A. (1980). A random flight model of inhomogeneous turbulent dispersion. *Physics of Fluids*, *23*(11), 2151–2153. doi:10.1063/1.862908

Dyer, A. J., & Bradley, E. F. (1982). An alternative analysis of flux-gradient relationships at the 1976 ITCE. *Boundary-Layer Meteorology*, *22*(1), 3–19. doi:10.1007/BF00128053

Feng, J. (2007). A 3-mode parameterization of below-cloud scavenging of aerosols for use in atmospheric dispersion models. *Atmospheric Environment*, *41*(32), 6808–6822. doi:10.1016/j.atmosenv.2007.04.046

Flesch, T. K., Wilson, J. D., & Yee, E. (1995). Backward-time Lagrangian stochastic dispersion models and their application to estimate gaseous emissions. *Journal of Applied Meteorology*, *34*(6), 1320–1332. doi:10.1175/1520-0450(1995)034<1320:BTLSDM>2.0.CO;2

Gerasopoulos, E., Zanis, P., Papastefanou, C., Zerefos, C. S., Ioannidou, A., & Wernli, H. (2006). A complex case study of down to the surface intrusions of persistent stratospheric air over the eastern Mediterranean. *Atmospheric Environment*, *40*(22), 4113–4125. doi:10.1016/j.atmosenv.2006.03.022

Girardi, F., Graziani, G., van Velzen, D., Galmarini, S., Mosca, S., Bianconi, R., … Fraser, G. (1998). The European Tracer Experiment (E. I. Joint Research Centre, Ed.). Office for Official Publications of the European Communities.

Gloster, J., Jones, A., Redington, A., Burgin, L., Sørensen, J. H., Turner, R., … Paton, D. (2010, 3). Airborne spread of foot-and-mouth disease –model intercomparison. *The Veterinary Journal*, *183*(3), 278–286. doi: 10.1016/j.tvjl.2008.11.011

Graziani, G., Klug, W., & Mosca, S. (1998). *Real-time long-range dispersion model evaluation of the ETEX first release*. EUR 17754 EN. Office for Official Publications of the European Community.

Gupta, S., McNider, R. T., Trainer, M., Zamora, R. J., Knupp, K., & Singh, M. P. (1997). Nocturnal wind structure and plume growth rates due to inertial oscillations. *Journal of Applied Meteorology*, *36*(8), 1050–1063. doi:10.1175/1520-0450(1997)036<1050:NWSAPG>2.0.CO;2

de Haan, P. (1999). On the use of density kernels for concentration estimations within particle and puff dispersion models. *Atmospheric Environment*, *33*(13), 2007–2021. doi:10.1016/S1352-2310(98)00424-5

Hanna, S. R. (1981). Lagrangian and Eulerian time-scale relations in the daytime boundary layer. *Journal of Applied Meteorology*, *20*(3), 242–249. doi: 10.1175/1520-0450(1981)020<0242:LAETSR>2.0.CO;2

Hanna, S. R. (1986). Spectra of concentration fluctuations: The two time scales of a meandering plume. *Atmospheric Environment (1967)*, *20*(6), 1131–1137. doi: 10.1016/0004-6981(86)90145-9

Haugen, D. A., Kaimal, J. C., & Bradley, E. F. (1971). An experimental study of Reynolds stress and heat flux in the atmospheric surface layer. *Quarterly Journal of the Royal Meteorological Society*, *97*(412), 168–180. doi: 10.1002/qj.49709741204

Hazi, Y., Heikkinen, M. S. A., & Cohen, B. S. (2003). Size distribution of acidic sulfate ions in fine ambient particulate matter and assessment of source region effect. *Atmospheric Environment*, *37*(38), 5403–5413. doi:10.1016/j.atmosenv.2003.08.034

Health Canada. (2014). *Federal nuclear emergency plan Part 1: Master plan federal* (5th Edition). Government of Canada. Retrieved from http://www.hc-sc.gc.ca/hc-ps/alt_format/pdf/pubs/ed-ud/fnep-pfun-1/PFUN-FNEP-2014-eng.pdf

ICAO. (2004). *Handbook of the International Airways Volcano Watch (IAVW) - Operational Procedures and Contact List*, (Second Edition) Montreal, Canada. Retrieved from http://www.icao.int/safety/meteorology/iavwopsg/Handbook%20on%20the%20I AVW%20Doc%209766/Forms/AllItems.aspx

Joly, A., Smargiassi, A., Kosatsky, T., Fournier, M., Dabek-Zlotorzynska, E., Celo, V., … Brook, J. (2010). Characterisation of particulate exposure during fireworks displays. *Atmospheric Environment*, *44*(34), 4325–4329. doi: 10.1016/j.atmosenv.2009.12.010

Katata, G., Ota, M., Terada, H., Chino, M., & Nagai, H. (2012). Atmospheric discharge and dispersion of radionuclides during the Fukushima Dai-ichi Nuclear Power Plant accident. Part I: Source term estimation and local-scale atmospheric dispersion in early phase of the accident. *Journal of Environmental Radioactivity*, *109*, 103–113. doi: 10.1016/j.jenvrad.2012.02.006

Krasnoff, E., & Peskin, R. L. (1971). The Langevin model for turbulent diffusion. *Geophysical & Astrophysical Fluid Dynamics*, *2*(1), 123–146. doi: 10.1080/03091927108236054

Langevin, P. (1908). Sur la théeorie du mouvement brownien. *Comptes rendus hebdomadaires de l'Acadéemie des sciences* (Vol. 146, p. 530–533). Paris: Gauthier-Villars.

Legg, B. J., Raupach, M. R., & Coppin, P. A. (1986). Experiments on scalar dispersion within a model plant canopy, part III: An elevated line source. *Boundary-Layer Meteorology*, *35*(3), 277–302. doi:10.1007/BF00123645

Mailhot, J., Bélair, S., Benoit, R., Bilodeau, B., Delage, Y., Filion, L., … Tremblay, A. (1998). *Scientific description of the RPN Physics Library (CMC NWP Models Documentation)*. Dorval, QC, Canada: Canadian Meteorological Centre.

Mailhot, J., & Benoit, R. (1982). A finite-element model of the atmospheric boundary layer suitable for use with numerical weather prediction models. *Journal of the Atmospheric Sciences*, *39*(10), 2249–2266.

Maryon, R. H. (1998). Determining cross-wind variance for low frequency wind meander. *Atmospheric Environment*, *32*(2), 115–121. doi: 10.1016/S1352-2310(97)00325-7

Mercier, J.-F., Tracy, B., d'Amours, R., Chagnon, F., Hoffman, I., Korpach, E., … Ungar, R. (2009). Increased environmental gamma-ray dose rate during precipitation: A strong correlation with contributing air mass. *Journal of Environmental Radioactivity*, *100*(7), 527–533. doi:10.1016/j.jenvrad.2009.03.002

Mosca, S., Bianconi, R., Bellasio, R., Graziani, G., & Klug, W. (1998). ATMES-II: Evaluation of long-range dispersion models using 1st ETEX release data. Draft report prepared for the ETEX Symposium on Long-range Atmospheric Transport, Model Verification and Emergency Response, Vienna, 13-16 May 1997. Office for Official Publications of the European Communities.

Mosca, S., Graziani, G., Klug, W., Bellasio, R., & Bianconi, R. (1998). A statistical methodology for the evaluation of long-range dispersion models: An application to the ETEX exercise. *Atmospheric Environment*, *32*(24), 4307–4324. doi:10.1016/S1352-2310(98)00179-4

Nieuwstadt, F. T. M. (1984). The turbulent structure of the stable, nocturnal boundary layer. *Journal of the Atmospheric Sciences*, *41*(14), 2202–2216. doi: 10.1175/1520-0469(1984)041<2202:TTSOTS>2.0.CO;2

Nodop, K., Connolly, R., & Girardi, F. (1998). The field campaigns of the European Tracer Experiment (ETEX): Overview and results. *Atmospheric Environment*, *32*(24), 4095–4108. doi:10.1016/S1352-2310(98)00190-3

O'Brien, J. J. (1970). A note on the vertical structure of the eddy exchange coefficient in the planetary boundary layer. *Journal of the Atmospheric Sciences*, *27*(8), 1213–1215. doi:10.1175/1520-0469(1970)027<1213:ANOTVS>2.0.CO;2

Paquin, M., & D'Amours, R. (2005). An example of real-time emergency response: The SO_3 Release in Valleyfield, Quebec. In *Proceedings of the Twenty-Eighth Arctic and Marine Oilspill Program (AMOP) Technical Seminar [including sessions for the Twenty-Second Technical Seminar on Chemical Spills (TSOCS)]* (Vol. 2, pp. 735-743). Ottawa: Environment Canada.

Pudykiewicz, J. (1989). Simulation of the Chernobyl dispersion with a 3-D hemispheric tracer model. *Tellus B*, *41B*(4), 391–412. doi:10.1111/j.1600-0889.1989.tb00317.x

Pudykiewicz, J. A. (1998). Application of adjoint tracer transport equations for evaluating source parameters. *Atmospheric Environment*, *32*(17), 3039–3050. doi:10.1016/S1352-2310(97)00480-9

Rodean, H. C. (1996). Stochastic Lagrangian models of turbulent diffusion (No. 48). 45 Beacon Street, Boston, Massachusetts 02108: American Meteorological Society. doi: 10.1175/0065-9401-26.48.1

Sawford, B. L. (1985). Lagrangian statistical simulation of concentration mean and fluctuation fields. *Journal of Applied Meteorology*, *24*(11), 1152–1166. doi:10.1175/1520-0450(1985)024<1152:LSSOCM>2.0.CO;2

Seibert, P., & Frank, A. (2004). Source-receptor matrix calculation with a Lagrangian particle dispersion model in backward mode. *Atmospheric Chemistry and Physics*, *4*(1), 51–63. doi:10.1016/0960-1686(90)90004-7

Simpson, J. J., Berg, J. S., Hufford, G. L., Bauer, C., Pieri, D., & Servranckx, R. (2002). The February 2001 eruption of Mount Cleveland, Alaska: Case study of an aviation hazard. *Weather and Forecasting*, *17*(4), 691–704. doi:10.1175/1520-0434(2002)017<0691:TFEOMC>2.0.CO;2

Sinclair, L. E., Seywerd, H. C. J., Fortin, R., Carson, J. M., Saull, P. R. B., Coyle, M. J., … Hall, R. M. (2011). Aerial measurement of radioxenon concentration off the west coast of Vancouver Island following the Fukushima reactor accident. *Journal of Environmental Radioactivity*, *102*(11), 1018–1023. doi: 10.1016/j.jenvrad.2011.06.008

Smith, F. B. (1965). The role of wind shear in horizontal diffusion of ambient particles. *Quarterly Journal of the Royal Meteorological Society*, *91*(389), 318–329. doi: 10.1002/qj.49709138906

Sparks, R., Bursik, M., Carey, S., Gilbert, J., Glaze, L., Sigurdsson, H., & Woods, A. (1997). *Volcanic plumes*. Baffin Lane, Chichester, West Sussex PO19 1UD, England: John Wiley & Sons. p. 384.

Stohl, A., Forster, C., Frank, A., Seibert, P., & Wotawa, G. (2005). Technical note: The Lagrangian particle dispersion model FLEXPART version 6.2. *Atmospheric Chemistry and Physics*, *5*(9), 2461–2474. doi: 10.5194/acp-5-2461-2005

Stohl, A., Seibert, P., Wotawa, G., Arnold, D., Burkhart, J. F., Eckhardt, S., … Yasunari, T. J. (2012). Xenon-133 and caesium-137 releases into the atmosphere from the Fukushima Dai-ichi nuclear power plant: Determination of the source term, atmospheric dispersion, and deposition. *Atmospheric Chemistry and Physics*, *12*(5), 2313–2343. doi: 10.5194/acp-12-2313-2012

Stohl, A., & Thomson, D. J. (1999). A density correction for Lagrangian particle dispersion models. *Boundary-Layer Meteorology*, *90*, 155–167. doi:/10.1023/A:1001741110696

Taylor, G. I. (1922). Diffusion by continuous movements. *Proceedings of the London Mathematical Society*, *s2-20*(1), 196–212. Retrieved from http://plms.oxfordjournals.org

TEPCO. (2012). The great east Japan earthquake and current status of nuclear power stations. Retrieved from http://www.tepco.co.jp/en/nu/fukushima-np/f1/images/f12np-gaiyoue1.pdf

Terada, H., Katata, G., Chino, M., & Nagai, H. (2012). Atmospheric discharge and dispersion of radionuclides during the Fukushima Dai-ichi Nuclear Power Plant accident. Part II: Verification of the source term and analysis of regional-scale atmospheric dispersion. *Journal of Environmental Radioactivity*, *112*(0), 141–154. doi: 10.1016/j.jenvrad.2012.05.023

Thompson, R. (1971). Numeric calculation of turbulent diffusion. *Quarterly Journal of the Royal Meteorological Society*, *97*(411), 93–98. doi: 10.1002/qj.49709741109

Thomson, D. J. (1984). Random walk modelling of diffusion in inhomogeneous turbulence. *Quarterly Journal of the Royal Meteorological Society*, *110*(466), 1107–1120. doi:10.1002/qj.49711046620

Thomson, D. J. (1987). Criteria for the selection of stochastic models of particle trajectories in turbulent flows. *Journal of Fluid Mechanics*, *180*, 529–556. doi:10.1017/S0022112087001940

Thomson, D. J., & Wilson, J. D. (2012). History of Lagrangian stochastic models for turbulent dispersion. In *Lagrangian modeling of the atmosphere* (pp. 19–36). Washington: American Geophysical Union. doi:10.1029/2012GM001238

Warner, S., Platt, N., & Heagy, J. F. (2004). Application of user-oriented measure of effectiveness to transport and dispersion model predictions of the European Tracer Experiment. *Atmospheric Environment*, *38*(39), 6789–6801. doi: 10.1016/j.atmosenv.2004.09.024

Weil, J. C. (1990). A diagnosis of the asymmetry in top-down and bottom-up diffusion using a Lagrangian stochastic model. *Journal of the Atmospheric Sciences*, *47*(4), 501–515. doi:10.1175/1520-0469(1990)047<0501:ADOTAI>2.0.CO;2

Wilson, J., Ferrandino, F., & Thurtell, G. (1989). A relationship between deposition velocity and trajectory reflection probability for use in stochastic

Lagrangian dispersion models. *Agricultural and Forest Meteorology*, *47*(2-4), 139–154. doi:10.1016/0168-1923(89)90092-0

Wilson, J., & Yee, E. (2007). A critical examination of the random displacement model of turbulent dispersion. *Boundary-Layer Meteorology*, *125*(3), 399–416. doi:10.1007/s10546-007-9201-x

Wilson, J. D. (2000). Trajectory models for heavy particles in atmospheric turbulence: Comparison with observations. *Journal of Applied Meteorology*, *39*(11), 1894–1912. doi:10.1175/1520-0450(2000)039<1894:TMFHPI>2.0.CO;

Wilson, J. D., & Flesch, T. K. (1993). Flow boundaries in random-flight dispersion models: Enforcing the well-mixed condition. *Journal of Applied Meteorology*, *32*(11), 1695–1707. doi:10.1175/1520-0450(1993)032<1695:FBIRFD>2.0.CO;2

Wilson, J. D., & Flesch, T. K. (2004). An idealized mean wind profile for the atmospheric boundary layer. *Boundary-Layer Meteorology*, *110*(2), 281–299. doi: 10.1023/A:1026044025803

Wilson, J. D., Flesch, T. K., & d'Amours, R. (2001, 02 01). Surface delays for gases dispersing in the atmosphere. *Journal of Applied Meteorology*, *40*(8), 1422–1430. doi: 10.1175/1520-0450(2001)040<1422:SDFGDI>2.0.CO;2

Wilson, J. D., Flesch, T. K., & Swaters, G. E. (1993). Dispersion in sheared Gaussian homogeneous turbulence. *Boundary-Layer Meteorology*, *62*(1), 281–290. doi:10.1007/BF00705559

Wilson, J. D., Legg, B. J., & Thomson, D. J. (1983). Calculation of particle trajectories in the presence of a gradient in turbulent-velocity variance. *Boundary-Layer Meteorology*, *27*(2), 163–169. doi:10.1007/BF00239612

Wilson, J. D., & Sawford, B. L. (1996, 10 01). Review of Lagrangian stochastic models for trajectories in the turbulent atmosphere. *Boundary-Layer Meteorology*, *78*(1), 191–210. doi: 10.1007/BF00122492

Wilson, J. D., Thurtell, G. W., & Kidd, G. E. (1981a). Numerical simulation of particle trajectories in inhomogeneous turbulence, III: Comparison of predictions with experimental data for the atmospheric surface layer. *Boundary-Layer Meteorology*, *21*(4), 443–463. doi:10.1007/BF02033593

Wilson, J. D., Thurtell, G. W., & Kidd, G. E. (1981b). Numerical simulation of particle trajectories in inhomogeneous turbulence, I: Systems with constant turbulent velocity scale. *Boundary-Layer Meteorology*, *21*(3), 295–313. doi:10.1007/BF00119275

Witham, C. S., Hort, M. C., Potts, R., Servranckx, R., Husson, P., & Bonnardot, F. (2007, 11 01). Comparison of VAAC atmospheric dispersion models using the 1 November 2004 Grimsvötn eruption. *Meteorological Applications*, *14*(1), 27–38. doi:10.1002/met.3

WMO. (2010, updated 2012). Manual on the global data-processing and forecasting system, Volume 1, Global Aspects (Appendix I-6, Regional and global arrangements for atmospheric backtracking; Appendix II-9, Products provided by RSMCS with activity specialization in atmospheric transport modelling – backtracking for CTBT verification support). 7 bis, avenue de la Paix, Geneva, Switzerland. Retrieved from http://www.wmo.int/pages/prog/www/DPFS/Manual_GDPFS.html

Wotawa, G., Geer, L.-E. D., Denier, P., Kalinowski, M., Toivonen, H., D'Amours, R., … Yamazawa, H. (2003). Atmospheric transport modelling in support of CTBT verification–overview and basic concepts. *Atmospheric Environment*, *37*(18), 2529–2537. doi:10.1016/S1352-2310(03)00154-7

Wyngaard, J. C. (2010). *Turbulence in the atmosphere*. Cambridge, UK: Cambridge University Press.

Yee, E., Lien, F.-S., Keats, A., & D'Amours, R. (2008). Bayesian inversion of concentration data: Source reconstruction in the adjoint representation of atmospheric diffusion. *Journal of Wind Engineering and Industrial Aerodynamics*, *96*(10–11), 1805–1816. doi:10.1016/j.jweia.2008.02.024